On the Role of Inertial Instability in Stratosphere–Troposphere Exchange near Midlatitude Cyclones*

SHELLIE M. ROWE AND MATTHEW H. HITCHMAN

Department of Atmospheric and Oceanic Sciences, University of Wisconsin–Madison, Madison, Wisconsin

(Manuscript received 19 July 2014, in final form 28 January 2015)

ABSTRACT

In simulations of midlatitude cyclones with the University of Wisconsin Nonhydrostatic Modeling System (UWNMS), mesoscale regions with large negative absolute vorticity commonly occur in the upper troposphere and lower stratosphere (UTLS), overlying thin layers of air with stratospheric values of ozone and potential vorticity (PV). These locally enhanced stratosphere–troposphere exchange (STE) events are related to upstream convection by tracing negative equivalent potential vorticity (EPV) anomalies along back trajectories. Detailed agreement between the patterns of negative absolute vorticity, PV, and EPV—each indicators of inertial instability in the UTLS—is shown to occur in association with enhanced STE signatures. Results are presented for two midlatitude cyclones in the upper Midwest, where convection develops between the subpolar and subtropical jets.

Mesoscale regions of negative EPV air originate upstream in the boundary layer. As they are transported through convection, EPV becomes increasingly negative toward the tropopause. In association with the arrival of each large negative EPV anomaly, a locally enhanced poleward surge of the subpolar jet occurs, characterized by high turbulent kinetic energy and low Richardson number. Isosurfaces of wind speed show that gravity waves emanating from inertially unstable regions connect with and modulate the subpolar and subtropical jets simultaneously. Inertially unstable convective outflow surges can facilitate STE locally by fostering poleward acceleration in the UTLS, with enhanced folding of tropospheric air over stratospheric air underneath the poleward-moving jet.

1. Introduction

a. Motivation

Stratosphere–troposphere exchange (STE) of air in the upper troposphere and lower stratosphere (UTLS) is an essential part of the Brewer–Dobson circulation, influencing the distribution of ozone, water vapor, and other constituents. An abrupt increase in static stability occurs at the tropopause because of the combined effects of stratospheric ozone heating and surface heating, with buoyant adjustment in the troposphere (e.g., Manabe and Wetherald 1967). The extratropical tropopause is defined to occur when the lapse rate is less than $2\,\mathrm{K\,km^{-1}}$ but is also well characterized by values of Ertel's potential vorticity [PV $= (1/\rho)(\partial\theta/\partial z)(f + \zeta)$, where ρ is density, θ is potential temperature, f is the Coriolis parameter, and ζ is relative vorticity] in the range ~(1–4) PVU (1 PVU $= 10^{-6}\,\mathrm{K\,kg^{-1}\,m^2\,s^{-1}}$) and by an ozone mixing ratio in the range of 100–200 ppbv. Diabatic and frictional processes are required for molecules to cross a material surface, such as the tropopause (Andrews et al. 1987; Haynes et al. 1991). Such processes occur in the vicinity of thunderstorm tops, 3D Rossby wave breaking (RWB), and in breaking gravity waves (Holton et al. 1995). Estimates of STE vary by more than a factor of 2 (e.g., Stohl et al. 2003), which highlights the need for improved understanding of the underlying dynamics.

The present work is motivated by our diagnosis of enhanced STE in conjunction with regions of inertial instability in simulations of many different midlatitude cyclones with the University of Wisconsin Nonhydrostatic

Denotes Open Access content.

* Supplemental information related to this paper is available at the Journals Online website: http://dx.doi.org/10.1175/JAS-D-14-0210.s1.

Corresponding author address: Matthew H. Hitchman, Department of Atmospheric and Oceanic Sciences, 1225 W. Dayton Street, University of Wisconsin–Madison, Madison, WI 53706.
E-mail: matt@aos.wisc.edu

DOI: 10.1175/JAS-D-14-0210.1

Modeling System (UWNMS). These simulations were carried out to investigate wintertime quasi-stationary precipitation features and to better understand the origin of the thin sheets (~hundreds of meters thick) of stratospheric air, which appear to curl poleward and downward into the troposphere near midlatitude jets in association with midlatitude Rossby wave breaking (e.g., Danielsen 1968). High-resolution dropwindsonde data sampling a wide variety of geographical locations and jet configurations, including cutoff lows [Fig. 4 in Shapiro (1974)], southeastward jets [Fig. 5 in Shapiro (1978); Fig. 3 in Shapiro (1980)], a digging trough [Fig. 1 in Shapiro (1981)], an Icelandic low [Fig. 4 in Shapiro (1985)], and a staircase of westerly jets [Fig. 16, Shapiro et al. (1987)], illustrate the ubiquitous sharpness and typical structure of stratospheric intrusions. Aircraft campaigns, satellite data analysis, and model analysis of trace constituents have shown that these sheets of air tend to be turbulent and exhibit a mixed stratospheric–tropospheric chemical signal (e.g., Browell et al. 1987; Zahn et al. 2000; Hoor et al. 2002; Stohl et al. 2003; Bowman et al. 2007; Pan et al. 2007; Hegglin et al. 2008). The mystery of how thin stratospheric intrusions are formed strongly motivates the present work.

In examining simulations of quasi-stationary, banded precipitation events in the upper Midwest with the UWNMS, regions of negative equivalent potential vorticity (EPV) were found near the tropopause on the anticyclonic-shear side of the jet in the model. As will be demonstrated, negative EPV in the UTLS (where it is statically stable and very dry) implies inertial instability. Adjacent to these negative EPV regions were found layers of turbulently mixed air associated with folds in PV and ozone. In this paper, we explore the hypothesis that mesoscale regions of inertial instability near the jet can facilitate STE. The proposed mechanism for STE is that inertial instability enhances poleward acceleration of air in the UTLS, overriding stratospheric air, creating the local signature of a fold or stratospheric intrusion, with enhanced shear, divergence, and mesoscale motions at the boundary between the two air masses leading to enhanced turbulent exchange.

b. *RWB, inertial instability, and westerly jets*

The subtropical westerly jets, which result from a buoyancy-driven redistribution of angular momentum by local Hadley circulations, are collocated with strong baroclinic energy conversion processes, as synoptic-scale Rossby waves amplify, break, and are absorbed in the UTLS (Andrews et al. 1987). RWB occurs in 3D, with occlusion involving both a reversal of the normally positive meridional gradient of PV and tropopause folds. RWB implies a cascade of energy to smaller scales, with small-scale mixing and radiative damping required for wave absorption (e.g., McIntyre and Palmer 1983). Convective, Kelvin–Helmholtz, inertial, and baroclinic instabilities tend to generate gravity waves. Gravity waves also amplify, break, and are absorbed through small-scale mixing and radiative damping. Turbulence from breaking waves and instability is required for STE. Over eastern North America it is common to find a subpolar jet near 300 hPa (315–330 K) in close proximity with a subtropical westerly jet near 200 hPa (340–350 K) (C. E. Christenson and J. E. Martin 2014, personal communication), key background ingredients for the present case studies.

A discussion of cyclonic and anticyclonic RWB, together with transport pathways in midlatitude cyclones, is given by Thorncroft et al. (1993). In many storms, a distinctive branch of the warm conveyor belt (WCB) curves cyclonically, riding up and over part of the lower stratosphere. This process can help us understand the dynamical cause of multiple tropopauses (e.g., Randel et al. 2007). The dry stratospheric conveyor belt (DCB), which typically curves cyclonically equatorward into the troposphere, can aid the formation of stratospheric intrusions by differential advection. Stratospheric intrusions often take the form of elongated PV streamers, as seen at constant height, and thin sheets, as seen in cross sections. These dry intrusions are sometimes related to severe wind events at the surface (Browning and Reynolds 1994) and forest fire outbreaks (Zimet et al. 2007; Schoeffler 2013).

In quasigeostrophic theory, a preferred region of poleward and downward circulation is expected to occur near the jet entrance region (e.g., Markowski and Richardson 2010). Cold air advection along the UTLS jet axis has been shown to be compatible with sinking downstream of a trough at synoptic scales (Martin 2006; Lang and Martin 2010).

Sawyer (1949) explored the possible role of inertial or symmetric instability in the UTLS in modifying midlatitude cyclogenesis, jet stream behavior, and meridional circulations. It is now understood that inertial instability plays a role in establishing quasi-stationary precipitation bands in midlatitude cyclones (e.g., Bennetts and Hoskins 1979; Knox 2003) and phenomena on the edges of anticyclones (Stevens and Ciesielski 1986; Knox 1997).

Sato and Dunkerton (2002) showed that conditions are inertially unstable more than 20% of the time in the upper troposphere on the equatorward side of the subtropical westerly jet south of Japan during boreal winter. They found that the existence of distinctive layered perturbations in the UTLS corresponded with times of inertial instability. Schumacher and Schultz (2000) found that inertially unstable conditions are common in the subtropical troposphere. Knox and Harvey (2005)

compiled a climatology of inertial instability and RWB and found that it is inertially unstable over 2%–5% of the midlatitude UTLS at any given time.

Useful middle atmosphere dynamical analogies to the present situation may be found in the theoretical work of Dunkerton (1981, 1983) and observational–diagnostic studies by Hitchman et al. (1987) and Hayashi et al. (2002), in which inertial instability is shown to be associated with enhanced convergence/divergence patterns. In the middle atmosphere, planetary Rossby waves, refracting toward and breaking in the subtropics, encounter inertially unstable conditions, with meridional accelerations exciting distinctive convergence/divergence patterns. As RWB proceeds, air with anomalous PV is advected across the equator, with resultant inertial instability, acceleration, divergence, and 3D circulations. The associated divergence–convergence fields facilitate an enstrophy cascade during RWB and help to homogenize PV (O'Sullivan and Hitchman 1992). One of the notable features of O'Sullivan and Dunkerton's (1995) numerical investigation of inertia–gravity wave (IGW) generation during RWB is the patterns of divergence/convergence that correspond to the generation of IGW. In their study, IGW with characteristic vertical wavelengths of ~(2–3) km were very active near the "head" of the WCB, with absorption occurring in the lowest stratosphere. Considerable mixing is implied near the head of the WCB, resulting from these processes in the UTLS. Here, it is argued that regions of inertial instability in the UTLS can excite stronger divergence–convergence fields than would otherwise exist and, hence, can be focal regions for emanating gravity waves.

c. *Convective influences on STE near jets*

A salient aspect of this study is the role of convection and the WCB in baroclinic systems. Recent studies that explore the role of latent heating during WCB ascent in creating midtropospheric positive PV anomalies and upper-tropospheric negative PV anomalies include Pomroy and Thorpe (2000), Knippertz and Wernli (2010), Lang (2011), Schemm et al. (2013), and Madonna et al. (2014). Cooper et al. (2004) showed that penetration of stratospheric intrusions by convection can facilitate subsequent mixing into the troposphere. Homeyer et al. (2011) found that convection into stratospheric intrusions can yield a distinctive mixture of more than 125 ppmv H_2O and 100 ppbv O_3. Griffiths et al. (2000) argued that the PV anomaly associated with a fold can help to induce convection. Conversely, Lang (2011) showed that convection can lead to intensification of lower-stratospheric fronts.

An example of ozone STE associated with a convective complex over China in March 2001 is described by Hitchman et al. (2004) and Kittaka et al. (2004), where STE occurred via self-induced peripheral descent, similar to the circulation around an atomic explosion or idealized warm bubble simulation [e.g., Fig. 5 in Wicker and Skamarock (1998)]. The convective complex occurred in the westerly jet south of Japan, and thereby had access to high ozone in the UTLS on the poleward side of the jet. Aircraft and UWNMS diagnoses showed that air with high PV, high ozone, and very low water vapor curled downward and inward to ~6.5 km and promoted the decay phase of the complex. In the cases studied here, locally enhanced stratospheric intrusions immediately follow convective injection of negative PV or inertially unstable air in the UTLS. It will be argued that this paradigm of a vertical plume with circulation and mixing around its periphery may be usefully applied to the present cases dominated by inertial instability–enhanced poleward surges of air in the UTLS, facilitating STE.

Hoggatt and Knox (1998) studied an elevated convection event in the upper Midwest during 14 July 1995 and discovered that elongated bands of light rain tend to coincide with a narrow region of negative PV. Simulations of the event indicated a quadrupole checkerboard pattern in the vertical motion field, signifying inertial instability, as in the equatorial middle atmosphere. Schumacher et al. (2010) simulated quasi-stationary precipitation bands and found that they occurred in an environment with a well-mixed baroclinic boundary layer, positive convective available potential energy, and widespread negative PV. They argued that ascent caused by frontogenesis and banded moist convection produced narrow regions of negative absolute vorticity directly by the upward transport of low-momentum air. Convective bands initiated within the ascending branch of the secondary circulation were associated with elevated and near-surface frontogenesis. Schumacher et al. (2015) reexamined this case and confirmed that the minor rainbands to the north of the low likely resulted from the combined effects of sloping topography and the inherent effects of symmetric instability. Their work is explicit about the presence of negative PV and inertial instability on the poleward side of the surface cyclone and anticyclonic side of the jet. Their focus, however, was on the cause of the precipitation maximum and to compare simulated versus observed convective bands near complex terrain.

d. *Organization of paper*

Dynamical diagnostic quantities are introduced in section 2, while the data and simulations are described in section 3. In sections 4 and 5, two case studies modeled with the UWNMS are presented, which feature

pronounced, quasi-stationary, elongated precipitation bands common in the upper Midwest during winter and spring. The 3D relationship between the locations of the jets, negative EPV, meridional flow, upstream convection, and synoptic storm features is highlighted. The intimate temporal linkage between negative EPV anomalies, the signature of sharpened stratospheric intrusions, and gravity waves connecting the jets is shown in supplementary film loops. Case 2 features the signature of STE as seen in ozone, initialized in the UWNMS with globally assimilated ozone from the Goddard Earth Observing System (GEOS; Stajner et al. 2008). A summary statement of the proposed mechanism featuring a schematic diagram is given in section 6. It will be argued that inertial instability associated with convection in the WCB between the subpolar and subtropical jets can facilitate STE by causing ''overfolds'' in the UTLS, as part of the baroclinic energy conversion process arising from air masses of different density subject to gravity and rotation.

2. Dynamical diagnostics

a. *Inertial instability, absolute vorticity, and potential vorticity*

Inertial instability occurs when angular momentum decreases radially outward, as in flow between two rotating cylinders (Rayleigh 1917; Taylor 1923). When this criterion for instability is met, parcels accelerate and rearrange themselves, tending to stabilize the angular momentum profile. A spatial variation in acceleration will cause divergence–convergence patterns. Conversely, resistance to radial motion occurs when angular momentum increases radially outward. Knox (2003) provides a useful overview of inertial instability theory and related phenomena.

Consideration of radial parcel displacement δs in an axisymmetric vortex yields the oscillator equation:

$$\frac{\partial^2}{\partial t^2}\delta s = -f(f+\zeta)\delta s, \tag{1a}$$

with acceleration occurring (inertial instability) if the coefficient is negative:

$$f(f+\zeta) < 0, \tag{1b}$$

where $f = 2\Omega\sin\varphi$ and $\zeta = \partial v/\partial x - \partial u/\partial y$ is relative vorticity (Eliassen and Kleinschmidt 1957; Holton 2006). From the reference frame of Earth's rotation axis, absolute angular momentum per unit mass is given by $m = ru + r^2\Omega$, where $r = a\cos\varphi$, a is Earth's radius, u is zonal flow, and Ω is the angular frequency of Earth's rotation. This inertial instability criterion is related to Ertel's potential vorticity (PV) and the gradient of angular momentum on an isentropic surface, as follows:

$$f \times \mathrm{PV} = \frac{1}{\rho}\frac{\partial\theta}{\partial z} f(f+\zeta) = -\frac{1}{r}\nabla_\theta m < 0 \tag{2}$$

(Hoskins et al. 1985; Hitchman and Leovy 1986). Inertial instability occurs when there is anomalously signed PV for a given hemisphere, or anomalous absolute vorticity: that is, when angular momentum increases toward the planetary rotation axis. This criterion for instability is easier to satisfy near the equator, where f is small and angular momentum surfaces are parallel to the surface of Earth. In the Northern Hemisphere, where $f > 0$, the flow is inertially unstable if the absolute vorticity of the basic flow is negative: $f + \zeta < 0$. Large values of PV (e.g., stratospheric) imply a stronger angular momentum gradient and, hence, resistance to poleward displacement. Inviscid inertial instability will occur in sufficiently strong anticyclonic relative vorticity, which is common on the equatorward flank of a westerly jet (Knox 2003). Inertial instability implies a divergence–convergence pattern associated with parcel acceleration and deceleration at the edges of inertially unstable regions, which in turn implies 3D circulations, enhanced turbulence, and mixing (Dunkerton 1983; Jones and Thorpe 1992; O'Sullivan and Hitchman 1992).

b. *Equivalent potential vorticity*

Let us examine the implications of negative equivalent potential vorticity in the Northern Hemisphere:

$$\mathrm{EPV} = \frac{1}{\rho}\frac{\partial\theta_e}{\partial z}(f+\zeta) < 0, \tag{3a}$$

$$\text{where} \quad \theta_e = \theta\exp\left(\frac{Lw_s}{c_pT}\right), \tag{3b}$$

$L = 2.5\times10^{-6}\,\mathrm{J\,kg^{-1}}$ is the latent heat of condensation, w_s is saturation water vapor mixing ratio, $C_p = 1005\,\mathrm{J\,kg^{-1}\,K^{-1}}$ is specific heat at constant pressure, and T is temperature (Holton 2006). The variable θ_e allows for energy conservation between vapor phase change and internal energy. As an example of the potential for latent heating to affect static stability and therefore EPV, following upglide in a moist WCB and starting with $12\,\mathrm{g\,kg^{-1}}$ in the boundary layer, if w_s were reduced to 0, θ would increase by 32 K, with increases in θ being largest in the lower and middle troposphere. In the UTLS, water vapor mixing ratios ($\sim10^{-6}$) are reduced by four orders of magnitude relative to a humid boundary layer ($\sim10^{-2}$), implying that θ_e is very nearly equal to θ and that EPV is very nearly equal to PV.

Equation (3) shows that EPV is negative if the atmosphere is either moist statically unstable or if it is inertially unstable. Air that is moist statically unstable that is brought by convection to the base of the stratosphere will be statically stable, but it may still have negative EPV, implying that upstream convective instability can lead to downstream inertial instability.

To understand the origin of the negative EPV anomalies, we consider the PV tendency equation. Because of turbulent mixing and diabatic processes, PV will not be conserved (Andrews et al. 1987). In warm conveyor belts and thunderstorms, latent heating dominates. Following Pomroy and Thorpe (2000), considering the dominant vertical component, and ignoring frictional effects, the PV tendency equation becomes

$$\frac{d\mathrm{PV}}{dt} = \frac{1}{\rho}\left[\zeta\frac{\partial}{\partial z}\left(\frac{d\theta}{dt}\right)\right]. \tag{4}$$

In the cases to be shown, air found on the equatorward side of the subpolar westerly jet often originates in the moist boundary layer of a subtropical air mass. In considering how this air could facilitate STE, it is important to include water vapor phase changes in defining potential temperature used in calculating PV. Since convective updrafts occur where $\partial\theta_e/\partial z < 0$, it is possible for air with negative EPV to be created and transported into the upper troposphere, as dehydration causes EPV to asymptote to PV, preserving its negative value, with strong static stability at the base of the stratosphere implying inertial instability. The upward decrease of latent heating in the upper portion of thunderstorm updrafts can cause significant negative EPV anomalies.

EPV dynamics are a vital contributor in assessing conditions conducive to conditional symmetric instability (CSI). The concept of EPV has been widely used in studies of baroclinic systems since CSI was first introduced as a potential mechanism for the generation of frontal rainbands (Bennetts and Hoskins 1979; Emanuel 1979; Montgomery and Farrell 1991; Schumacher and Schultz 2000; Schultz and Knox 2007). EPV has proven useful in diagnosing squall lines (Zhang and Cho 1992), extratropical cyclones (Cao and Cho 1995; Cao and Zhang 2004; Brennan et al. 2008), convective snowstorms (Halcomb and Market 2003), and dynamics of the UTLS (Hoskins et al. 1985; Morgan 1999). The present paper focuses on the role of inertial instability in enhancing STE in the UTLS, as highlighted by regions of large negative EPV.

c. *Turbulent kinetic energy and Richardson number*

Turbulence and gravity waves are noticeably enhanced in the UTLS near westerly jets and play an important role in mixing (Lindzen and Tung 1976; Uccellini and Koch 1987; Pavelin et al. 2002; Whiteway et al. 2003; Duck and Whiteway 2005; Koch et al. 2005). Mixing near tropopause associated with breaking internal waves helps determine the distribution of trace gases (Clayson and Kantha 2008). Smith and Bernard (2013) showed that the forward cascade of buoyancy variance implies an enhanced region of turbulence near the tropopause.

The TKE and Ri patterns to be shown highlight regions of small-scale mixing, which facilitate the exchange of air between the stratosphere and troposphere. Kinetic energy per unit mass (TKE, $\varepsilon \sim \mathrm{m^2\,s^{-2}}$) is a measure of the intensity of turbulence and is defined as

$$\varepsilon = \frac{1}{2}(\overline{u'^2} + \overline{v'^2} + \overline{w'^2}), \tag{5}$$

where the overbar indicates time and space averaging of the turbulent eddy variances. The UWNMS includes a prognostic equation for TKE, including advection, buoyancy generation, shear generation, and turbulent dissipation (Tripoli 1992a,b).

Distributions of the Richardson number (Ri) highlight where convective or shear instability is generating TKE. The term Ri is the ratio of the mechanical generation of TKE by wind shear to the buoyancy production or inhibition by static stability:

$$\mathrm{Ri} = \frac{\dfrac{g}{\theta}\dfrac{\partial\theta}{\partial z}}{\left(\dfrac{\partial u}{\partial z}\right)^2 + \left(\dfrac{\partial v}{\partial z}\right)^2}, \tag{6}$$

where the numerator is equal to the square of the buoyancy frequency. The flow is dynamically unstable for flows with $\mathrm{Ri} < 0.25$ (e.g., Markowski and Richardson 2010). Once generated, turbulent flow tends to stay turbulent, even for Ri numbers as large as 1.0 (e.g., Stull 1988).

3. Data and analysis methods

During the course of simulating banded precipitation maxima in midlatitude cyclones with the UWNMS, distinctive mesoscale regions of negative EPV were often observed in the UTLS on the equatorward side of the subpolar jet. The spatial and temporal coincidence of pronounced mesoscale stratospheric intrusions on the poleward side of the jet, as seen in PV, θ, and ozone, suggested that perhaps the regions of negative PV were related to the locally enhanced STE. During 6–8 February 2008 (Case 1), phenomena of interest were located over south-central Wisconsin and northern Illinois. During 22–23 April 2005 (Case 2), negative EPV, poleward surges, and the signature of stratopause folds occurred over the Ohio Valley.

Each case is modeled with the UWNMS (Tripoli 1992a,b), initialized with 2.5° European Centre for Medium-Range Weather Forecasts (ECMWF) data. Studies of STE and other processes in the UTLS using the UWNMS include Pokrandt et al. (1996), Hitchman et al. (1999, 2003, 2004), Kittaka et al. (2004), and Büker et al. (2005, 2008). The specified UWNMS resolution for each case is 20 km × 20 km × 300 m, with a grid volume of 152 × 152 × 60 points. The top of the model is set to 16 km, with a 1500-m Rayleigh sponge layer. Each of the simulations was initialized ~24 h before the phenomena of interest began and continued for 48 h.

Case 2 was chosen in part because of the availability of high-quality globally assimilated ozone fields from GEOS data for 2005 (Stajner et al. 2008). GEOS ozone data are used to initialize the UWNMS and to update ozone on the UWNMS side boundaries. Detailed ozone structures evolve in the interior of the UWNMS over the subsequent 48 h.

The visualization software Vis5D was used to view the 3D structure of each midlatitude cyclone and the associated dynamical quantities in the UWNMS and to create trajectories that connect the negative EPV anomalies with upstream convection. A local archive of the 211-grid NAM model analyses from the National Centers for Environmental Prediction (NCEP), stored at 80-km resolution, was used to illustrate the broader synoptic context for the UWNMS simulations. These charts provide corroborating evidence of the prevalence of inertial instability on the equatorward side of the subpolar and subtropical jets.

4. Case study 1 (6–8 February 2008)

a. Synoptic overview

This destructive midwinter storm during 6–8 February 2008 featured quasi-stationary snowbands, which trapped over 2000 vehicles for 24 h on the Interstate 90 (I-90) highway in southern Wisconsin and spawned deadly tornadoes along the cold front throughout the Mississippi and Ohio Valleys. In addition to chronic negative absolute vorticity on the equatorward side of the subpolar jet, convection erupted along the cold front, injecting air into the UTLS between the subtropical and subpolar jets, generating EPV values of less than −3 PVU on the equatorward flank of the subpolar jet.

Figure 1 shows an overview of the synoptic-scale features in the lower troposphere associated with the storm at 0000 UTC 6 February 2008 using NCEP NAM model analyses. Figures 1a and 1b show the surface low pressure centered over southern Missouri and the associated baroclinic zone at 850 hPa. During the low's migration northeastward over Ohio, quasi-stationary snowbands matured and persisted in an arc-shaped pattern from southern Iowa into northern Illinois and southern Wisconsin, with snowfall in the range of 12–18 in., exceeding

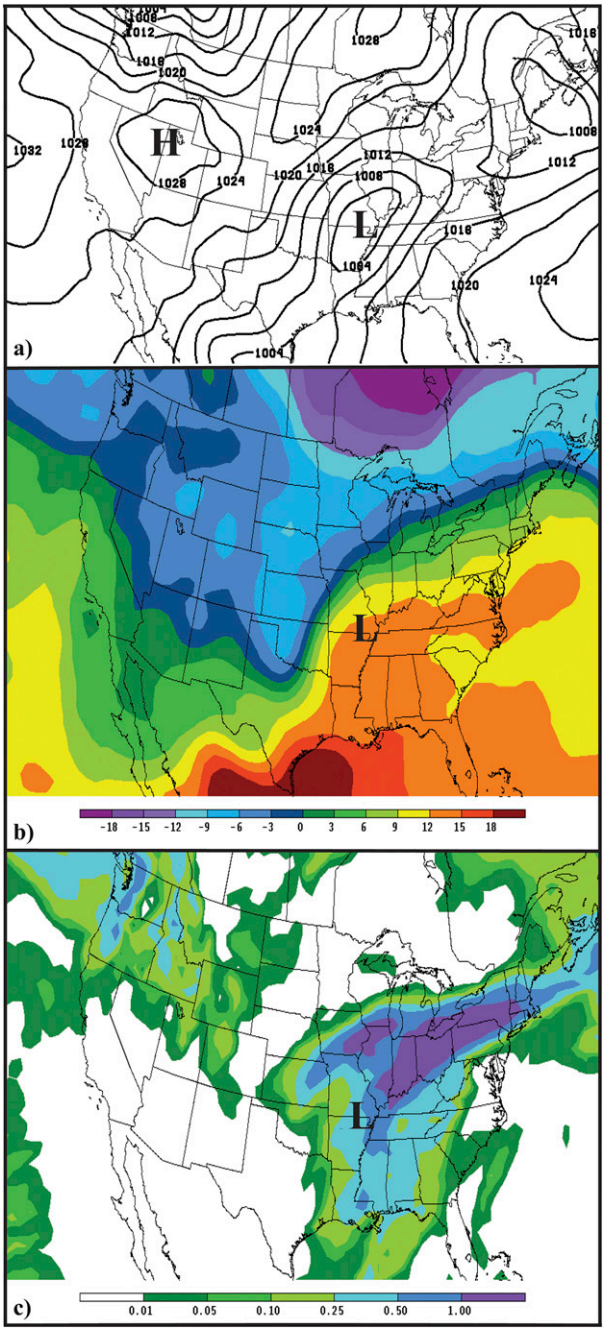

FIG. 1. Lower-tropospheric synoptic setting for Case 1, as seen in NCEP NAM model analyses at 0000 UTC 6 Feb 2008: (a) sea level pressure (black contours; interval: 4 hPa), (b) 850-hPa temperature (color bar; interval: 3°C), and (c) 24-h accumulated precipitation during 0000 UTC 6 –0000 UTC 7 Feb 2008 (color bar; in inches). The location of the surface low pressure center is indicated with an "L."

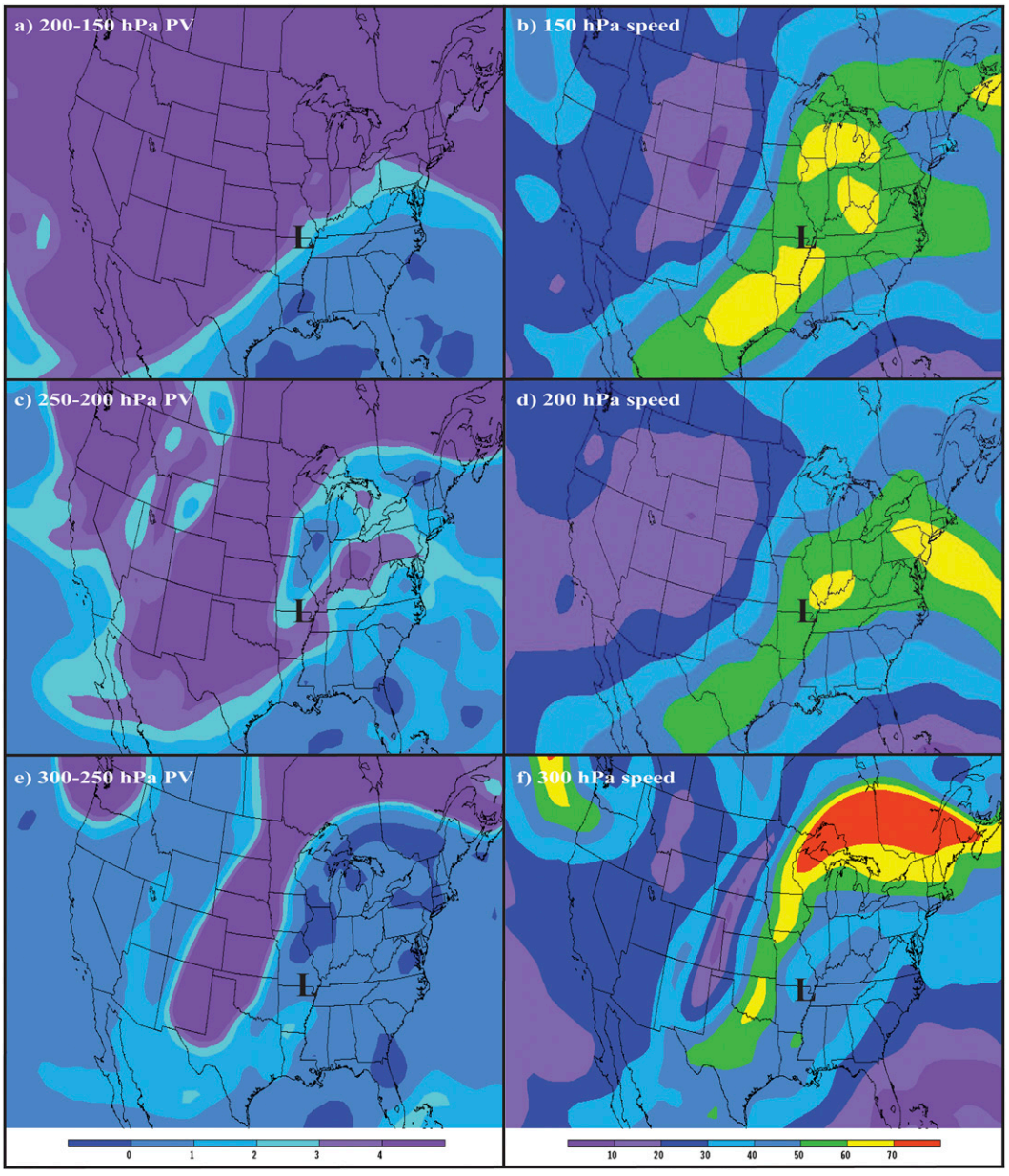

FIG. 2. As in Fig. 1, but for the UTLS synoptic setting for Case 1, showing (a),(c),(e) layer-averaged PV (color bar; interval: 1 PVU) and (b),(d),(f) wind speed (color bar; interval: 10 m s^{-1}) for (a) 200–150-hPa PV, (b) 150-hPa speed, (c) 250–200-hPa PV, (d) 200-hPa speed, (e) 300–250-hPa PV, and (f) 300-hPa speed.

1 in. water equivalent (Fig. 1c). This pattern is related to the cyclonic branch of the WCB.

Figure 2 depicts the distribution of PV and wind speed in the UTLS for the same time as in Fig. 1. At 300 hPa, a strong subpolar jet with speeds in excess of 70 m s^{-1} can be seen in Fig. 2f, arcing anticyclonically from Texas toward the Maritime Provinces, while at 200 and 150 hPa, (Figs. 2d,b), the subtropical jet can be seen extending from eastern Mexico toward the mid-Atlantic states. A pronounced southward extension of high polar stratospheric PV air in the 300–250-hPa layer is shown in purple in Fig. 1e, along with a broad anticyclonic arc of negative EPV in dark blue on the equatorward side of the subpolar jet (cf. Figs. 2e,f). The pattern of EPV in the 250–200-hPa layer includes negative regions over Illinois and southern Québec on the equatorward side of the subpolar jet (cf. Figs. 2c,d). The negative PV regions over the Gulf of Mexico and northern Florida occur on the equatorward side of the subtropical jet and become more extensive in area upon ascending

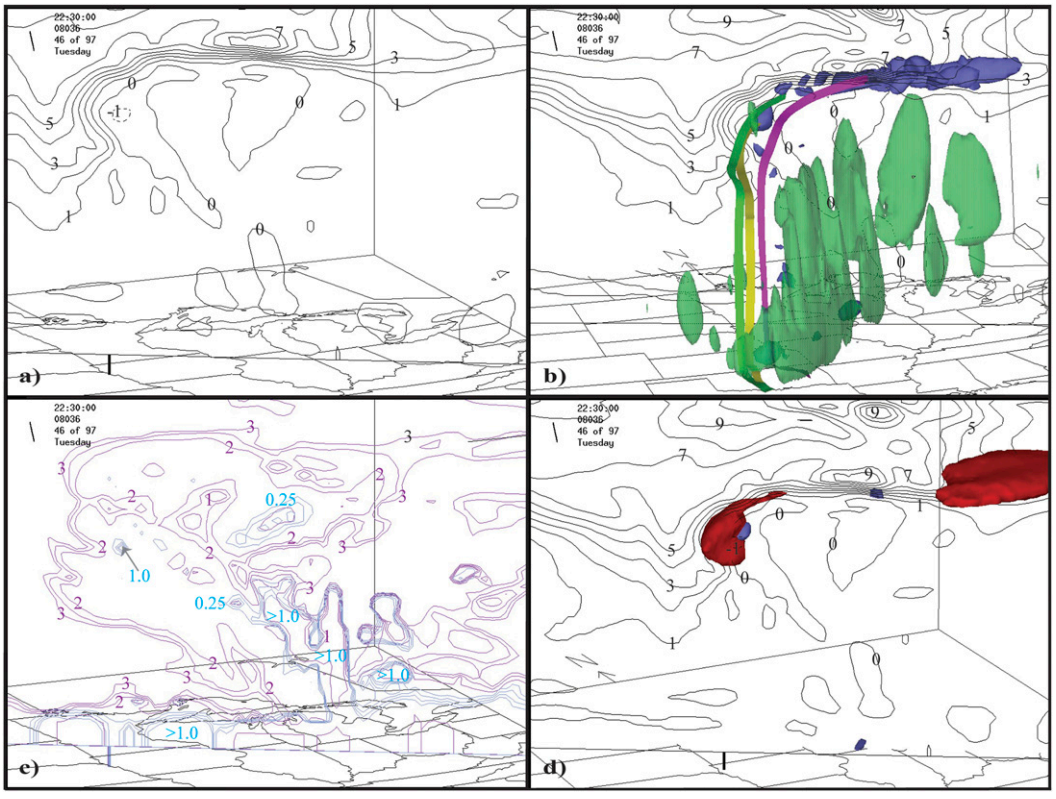

FIG. 3. The relationship among convection, inertial instability, jet locations, PV, and stratospheric intrusions in UWNMS Case 1 at 2230 UTC 6 Feb 2008, showing a view from the southwest of a vertical section extending from North Dakota, across the subpolar jet, to the subtropical jet over Kentucky. (a),(b),(d) EPV contours (gray; interval: 1 PVU) are shown. (b) Convection along the cold front is indicated with a green (4-cm s^{-1} upward motion) isosurface; the blue (−2 PVU) isosurfaces indicate regions of strong inertial instability in the UTLS; and the green, yellow, and magenta ribbons show 22.5-h back trajectories from these −2-PVU regions to where they spent the first 10 h in the unstable boundary layer over Kansas. (d) The two jets (red; 60-m s^{-1} isosurface) and the same blue −2-PVU isosurface as in (b), but values behind the section are not shown. (c) The vault of low Ri (purple contours; interval: 0.5; range: 0–3), and regions of high TKE (blue contours; interval: 0.25; range: 0–1.0).

from the 300–250-hPa layer to the 200–150-hPa layer (Figs. 2a,c,e).

In agreement with previous studies of the relationship between symmetric instability and regions of enhanced rainfall (e.g., Hoggatt and Knox 1998; Schumacher et al. 2010, 2015), the region of negative PV over northern Illinois and southern Wisconsin (Figs. 2c,e) coincides fairly well with the lobe of maximum 24-h precipitation seen in Fig. 1c.

b. *Overview of UWNMS Case 1*

Figure 3 shows an oblique view from the southeast of a section from North Dakota to western Virginia in the UWNMS simulation at 2230 UTC 6 February 2008. The distribution of EPV is shown in Figs. 3a, 3b, and 3d. Note the regions of negative EPV in the upper troposphere over Wisconsin and Illinois, adjacent to stratospheric air (1–6 PVU) over northwestern Minnesota. Figure 3d includes a 60-m s^{-1} speed isosurface (red), and isosurfaces of negative EPV exceeding −2 PVU (blue; excluding values from behind the section). Note the coincidence of the subpolar jet and region of inertial instability immediately adjacent to the stratospheric air. Note also the separation between the subpolar jet over Iowa and the higher-altitude subtropical jet over Kentucky in this section (Fig. 3d).

Figure 3b shows the relationship between the EPV distribution and regions of EPV exceeding −2 PVU on the equatorward side of the jet, as well as connections (back trajectory ribbons) to the surface via the WCB and convection along the cold front (4-cm s^{-1} green updraft isosurfaces). The regions of strongly negative EPV are seen to originate in the boundary layer over Kansas ~14 h earlier. A quantitative analysis of EPV evolution along the trajectory is given in the next subsection. The poleward buckling of EPV contours in the UTLS and enhanced signature of a stratospheric intrusion occurs with the arrival of inertially unstable air from convective outflow in the WCB.

The contemporaneous distribution of TKE (blue contours) and Richardson number (purple contours) is

shown in Fig. 3c. The region of EPV < 0 in the uppermost troposphere (Fig. 3a) generally coincides with low Ri and high TKE, with strong gradients along the base of the stratosphere over the jet core and into the troposphere along the upper edge of the stratospheric intrusion. It will be shown that there is a strong correspondence between the edge of the region of negative PV and low Ri and the location of enhanced divergence/convergence patterns. Note also the coincidence of TKE exceeding $1.0\,m^2\,s^{-2}$ and Ri < 1 in the convective element over Illinois.

The onset of the effects of inertial instability is depicted in Fig. 4. At 1300 UTC 6 February 2008 a broad jet with winds exceeding $60\,m\,s^{-1}$ occurred in the UTLS over Iowa (Fig. 4b), with the tropopause sloping gently and monotonically upward toward the south, as indicated by the 1-PVU contour (Fig. 4a) and transition to red (Fig. 4b). At this time, there were only modest regions of negative EPV near the jet (Fig. 4a). But by 1830 UTC, maximum wind speeds had increased to $75\,m\,s^{-1}$ and shifted poleward, in conjunction with the arrival of convective outflow air with PV < -2 PVU (Figs. 4c,d). By 2100 UTC, the region of strongly negative EPV had passed east of the section (Figs. 4e,f). This sequence shows that the tropopause undergoes a distinct folding process in association with the arrival of strongly inertially unstable air and a poleward surge in the UTLS, yielding the signature of tropospheric air overriding stratospheric air underneath the subpolar jet.

A comparison of the distributions of PV, angular momentum, wind speed, inertial instability, meridional streamfunction, and divergence is shown for 2100 UTC 6 February in Fig. 5. High values of angular momentum (divided by Earth's radius) are seen to bulge poleward in the UTLS in Figs. 5a–c, with the maximum poleward displacement coinciding with the jet maximum and with regions of strong inertial instability (EPV < -2 PVU; Fig. 5a). The total area of inertial instability is larger than the purple patches in Figs. 5a and 5d, as evidenced by the area over which m contours reverse sign (m increasing poleward from Missouri to Minnesota in the UTLS).

The $60\text{-}m\,s^{-1}$ jet isosurface is highlighted in light blue in Fig. 5b. Note the large region where $\partial m/\partial y > 0$ in the upper troposphere, tilting poleward with altitude into the jet. This enhanced region of strong inertial stability occurs at the head of the poleward surge in Figs. 5a–c.

The structure of the poleward surge is seen in Fig. 5c, with the greatest poleward motion occurring in the UTLS, coincident with the greatest poleward excursion of tropical m contours. This poleward surge is a blend of air from the subtropics and from convection along the cold front and extends well into the stratosphere.

A wedge of descending, equatorward flow exists in the lower troposphere, with the boundary between the two air masses tilting poleward with height. This differential advection in the meridional plane is a key ingredient in producing the signature of a stratospheric fold. The poleward convective outflow surge characterized by inertial instability overrides the layer of stratospheric air. This "sloping convection" signature of rising warm air and sinking cold air is to be expected for baroclinic synoptic waves.

The air at the top of the updraft (streamfunction in Fig. 5c) is strongly divergent in the UTLS (dashed contours in Fig. 5d) and is coincident with a region of negative EPV. Theory predicts poleward acceleration and, hence, horizontal divergence in a region of inertial instability and initial poleward motion (Dunkerton 1981, 1983; Hitchman et al. 1987; O'Sullivan and Hitchman 1992; O'Sullivan 1993; Hoggatt and Knox 1998). The upward-open V-shaped pattern of divergence and convergence in the troposphere in Fig. 5d will be shown to be related to the location of inertial instability and the generation of gravity waves, to be discussed below. A comparison of Fig. 5d with Figs. 3a,c shows that the edge of the vault of negative PV and low Ri coincides with a locus of enhanced divergence/convergence, facilitating mixing at the transition from stratospheric to tropospheric air.

An animation of this process is provided in supplemental movie 1 (available online), which highlights the intimate temporal relationship between the arrival of negative EPV anomalies in the UTLS, the poleward surges emanating from the regions of negative EPV, and the enhanced signature of a stratospheric intrusion resulting from overriding UTLS air. Figures 3–5 and S1 show that regions of negative EPV within the jet originate in upstream convection and are associated with poleward surges in the westerly jet. This association between negative absolute vorticity and turbulence variables suggests that inertial instability is associated with enhanced mixing of air, as well as with an enhanced intrusion signature. This provides evidence for the hypothesis that strong vertical motion associated with convection creates negative EPV air in the uppermost troposphere, with the resulting inertial instability favoring poleward flow and locally enhanced stratospheric intrusions.

c. *Changes of EPV along the path*

Negative anomalies of EPV can form because of diabatic processes associated with surface cooling or with latent heat release in regions of ascent (Morgan 1999). In convection embedded in the warm upglide sector, a latent heating maximum can generate negative PV through vortex shrinking (Joos and Wernli 2012). Figure 3b shows how updrafts transport unstable air from the surface into the jet, often yielding regions of

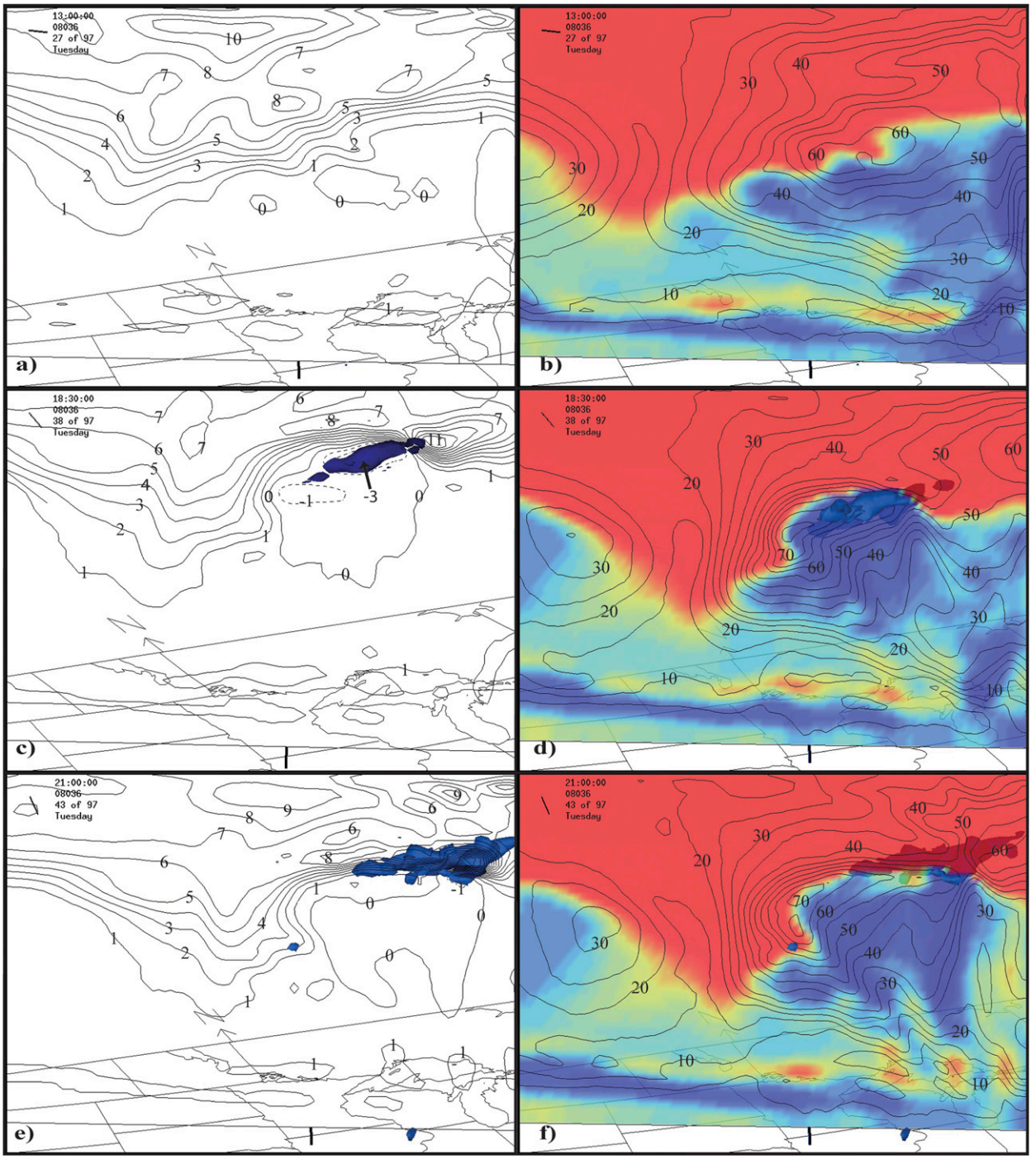

FIG. 4. Onset of the effects of inertial instability as seen in vertical sections of (left) PV, and (right) wind speed and regions of inertial instability in the UWNMS for (a),(b) 1300 UTC; (c),(d) 1830 UTC; and (e),(f) 2100 UTC on 5 Feb 2008. The PV is shown in (a),(c),(e) in black contours (interval 1 PVU), and in color in (b),(d),(f) [blue < 0 (inertially unstable); yellow 0–1; red > 1 (stratospheric air)]. Wind speed is contoured (interval: 5 m s^{-1}) in (b),(d),(f). A blue isosurface of strong inertial instability (EPV < -2 PVU) is seen entering the plane of the section from the west in (c) and (d) and exiting behind the plane in (e) and (f).

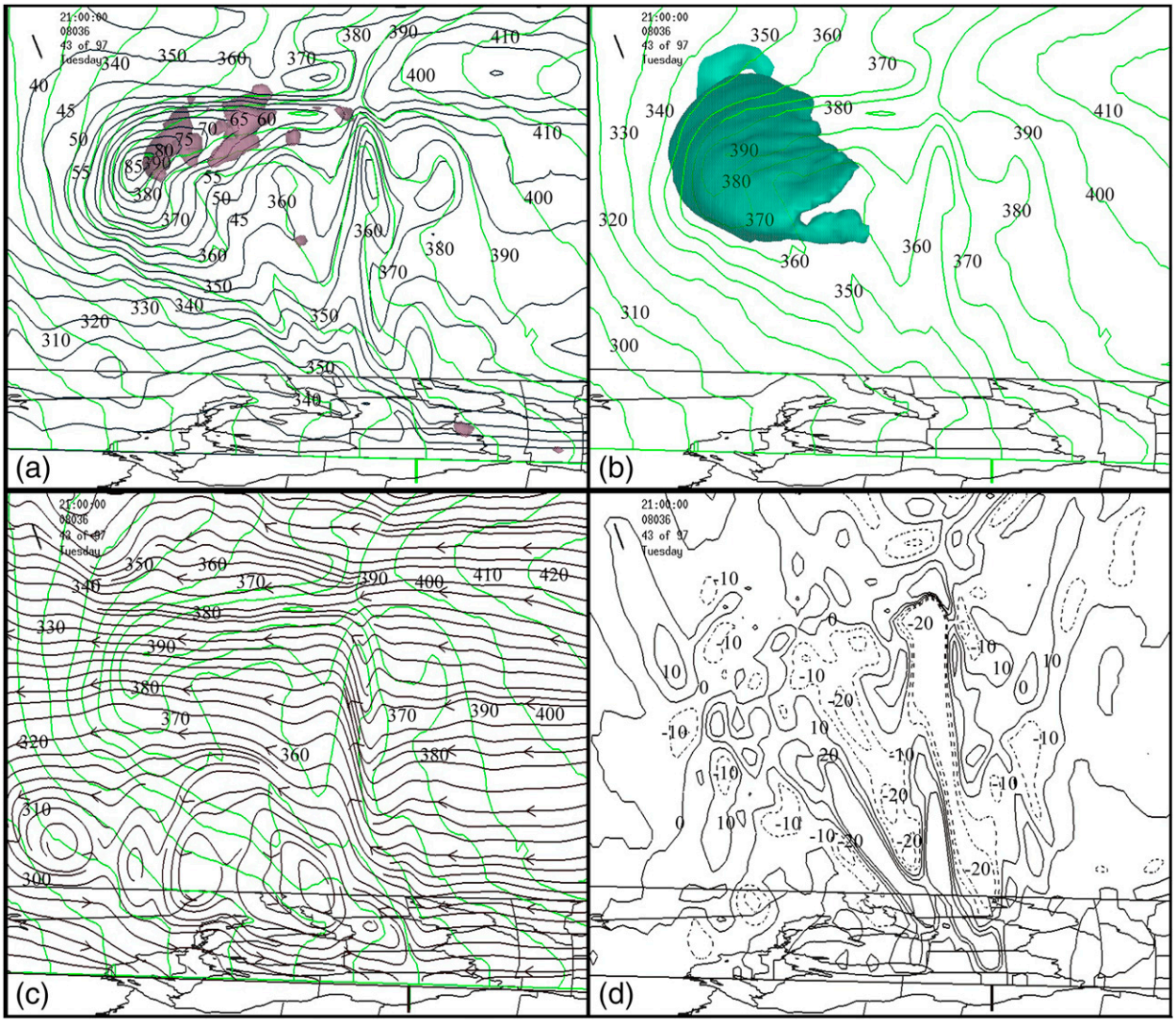

FIG. 5. Meridional sections showing the relationship between absolute angular momentum, wind speed, regions of inertial instability, divergence, and meridional streamfunction, as seen from the west in the UWNMS at 2100 UTC 5 Feb 2008. (a),(b),(c) Absolute angular momentum per unit mass divided by Earth's radius (green contours with 3-digit labels, every 10 m s^{-1}). (a) Zonal wind speed (gray contours with 2-digit labels, every 10 m s^{-1}), together with highly inertially unstable regions (EPV < -2 PVU in purple). (b) The collocation of the poleward-surging high-angular-momentum air mass and the 60-m s^{-1} wind speed isosurface (in aquamarine). (c) Meridional streamfunction (in gray), indicating the depth of the poleward intrusion. (d) Regions of convergence (solid) and divergence (dashed), with contours at $\pm 10 \times 10^{-5}$ s^{-1} and $\pm 20 \times 10^{-5}$ s^{-1}.

negative EPV exceeding -3 PVU at heights near 11 km. The negative EPV air found equatorward of the jet initially resided near the surface before being transported to the base of the stratosphere via updrafts exceeding 4 cm s^{-1}. These negative EPV anomalies are typically ~1 km thick (3–4 vertical grid points), with the horizontal scale varying from ~40 to 200 km (2–10 grid points). Back trajectories in Fig. 3 reveal the origin of the negative EPV anomalies in the unstable boundary layer as they become increasingly more negative above the heating maximum in the midtroposphere.

The probe function in Vis5d allows for sampling model variables along the trajectories in this WCB region, including changes of EPV and net diabatic heating along the path.

A negative EPV anomaly typically originates near the surface, with values around 0 PVU. As the air rises into the upper troposphere, EPV becomes more negative, exceeding -3 PVU on the equatorward side of the subpolar jet. By considering Eqs. (3) and (4), one may estimate changes in PV due to the pattern of latent heating. The density factor favors larger EPV anomalies in the upper troposphere. Since latent heating maximizes in the midtroposphere, then

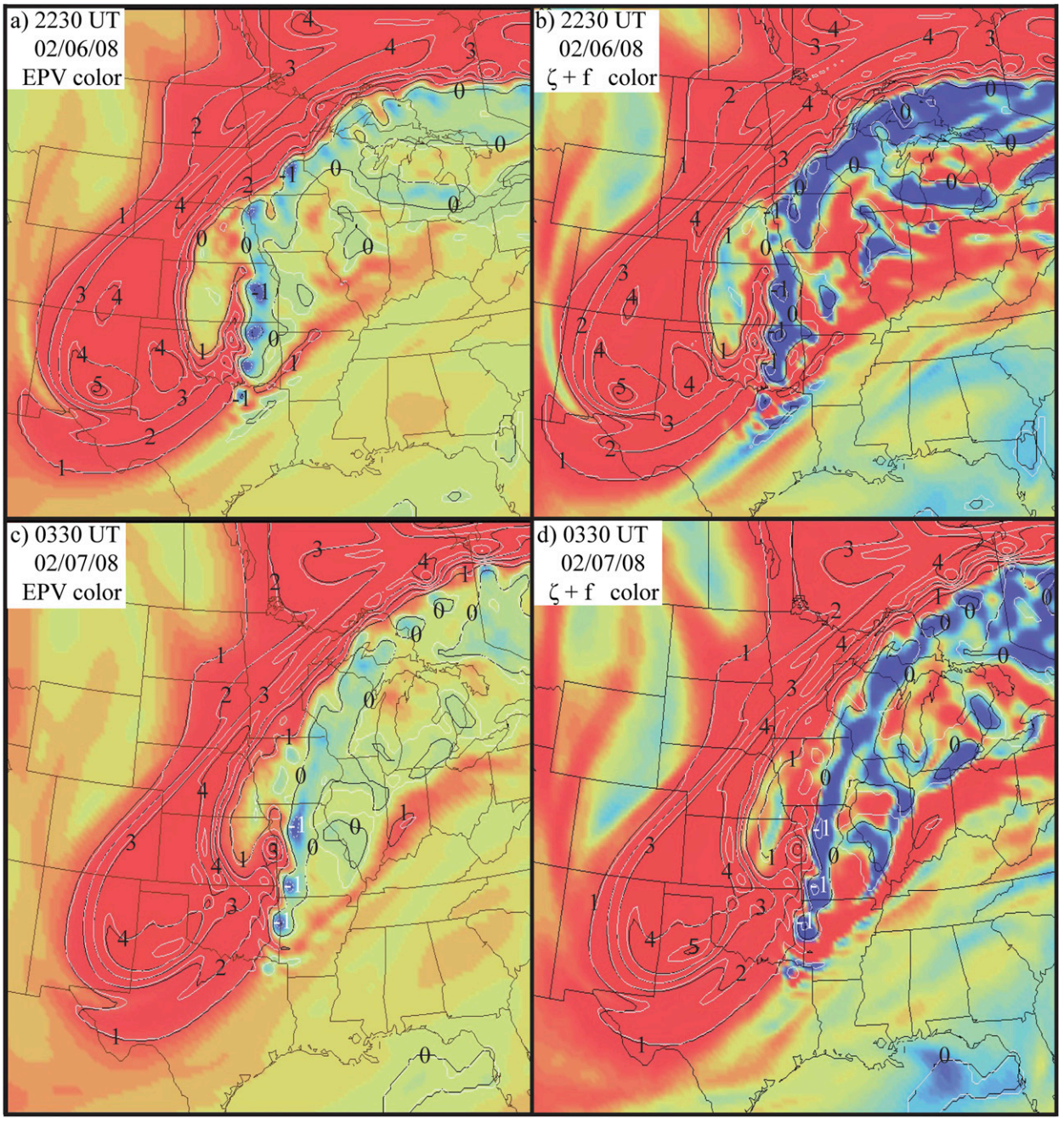

FIG. 6. Evolution of PV at 8 km in the UWNMS from (a),(b) 2230 UTC 5 to (c),(d) 0330 UTC 6 Feb 2008. PV (EPV) contours are shown in black (white) (interval: 1 PVU). For each time, (left) EPV and (right) absolute vorticity ($10^{-5}\,s^{-1}$) are shown in color. The color ranges are blue [<0 (inertially unstable)], yellow (0–1), and red [>1 (stratospheric air)].

$\partial(d\theta/dt)/\partial z < 0$ in the upper troposphere, generating negative PV. If a latent heating maximum of 20 K $(6\,h)^{-1}$ is assumed near 600 hPa, Eq. (4) suggests that with $\rho \sim 0.3\,kg\,m^{-3}$, $f \sim 10^{-4}\,s^{-1}$, and $\delta z \sim 4000$ m, an EPV anomaly of ~ -3 PVU could be generated approaching the 200-hPa level. This calculation supports the mechanism of generating negative EPV described by previous authors.

d. Evolution and comparison of PV, EPV, and absolute vorticity at 8 km

Figure 6 shows a quantitative comparison of PV, EPV, and absolute vorticity at 8 km and their evolution leading up to the time shown in Fig. 3. The detailed quantitative agreement between PV, EPV, and absolute

vorticity at this level shows that spatial variations in relative vorticity dominate and that spatial variations in dry static stability and moisture are relatively minor. The predominant pattern in Fig. 3 is the horizontal signature of RWB in the UTLS. The lobe of stratospheric air over Minnesota is part of an elongated broad filament of high-PV air extending over Texas, exhibiting vortex roll-up at its tip. The slow progression of this digging trough was instrumental in causing the quasi-stationary weather phenomena of this Super Tuesday outbreak. The subpolar jet stream follows the edge of the main stratospheric high-PV filament at 8 km, attended by a locus of inertially unstable air arcing from eastern Oklahoma over Wisconsin and toward Québec. The base of the subtropical jet follows the edge of the thin PV filament arcing over Ohio (cf. Figs. 2 and 6). The region between these two jets is characterized by the convective vault of low PV in the WCB.

The detailed spatial coincidence of negative regions (blue) of EPV and absolute vorticity shows that in the UTLS, either variable may be taken as a reliable indicator of inertial instability and, hence, may be useful in anticipating enhanced mesoscale motions, such as radiation of internal gravity waves. The region of low PV over the upper Midwest seen in Fig. 6 corresponds to the vault of low PV and low Ri in Fig. 3 and the upward-opening V-shaped pattern of divergence–convergence in Fig. 5d. The relatively narrow (~100 km wide) arc of strong inertial instability extending from Oklahoma into Canada on the equatorward side of the subpolar jet in Fig. 6 is characterized by mesoscale bead-like enhancements. This feature is a focal region for generating IGWs, as described in the next section.

e. *A case of ''jet suturing'' via gravity waves excited by inertial instability?*

Figures 7 and 8 show the evolution of the jet pair from the southwest and east, respectively. Supplemental movies 2 and 3 show the evolution of this jet pair for the 48-h simulation, as seen from the west and the east. In this sequence, poleward- and upward-moving streams of air with EPV < -1 PVU are highlighted in aquamarine, while the 55-m s^{-1} speed isosurface is shown in yellow. Figures 7b, 7d, and 7f include horizontal sections of absolute vorticity at 5 km. The narrow blue arc of inertial instability at 5 km underlies the narrow arc of inertial instability seen at 8 km in Fig. 6. The air masses with large negative EPV are seen to travel upward and northeastward through an elongated band of negative absolute vorticity at 5 km, connecting to downward-extending fingerlike structures of high wind speed from both jets. This mesoscale disturbance is related directly to the convection and locus of inertial instability. The fingers of high wind speed have their roots in the beaded, long thin arc of negative absolute vorticity (Fig. 6). This mesoscale wave pattern fans out in the vertical, compatible with the convergence–divergence pattern in Fig. 5d, and embraces both jets in the UTLS, modulating them simultaneously. These inertia–gravity waves generated by the convection and inertial instability appear to join the subtropical and subpolar jets together, in a rib-like or suture pattern. This result is reminiscent of the work of O'Sullivan (1993), who explored the relationship between IGW, the midlatitude tropospheric jet, and the polar night jet.

The predominant gravity waves shown in Figs. 7 and 8, and the spacing of the beads of negative PV in Fig. 6, appear to have horizontal wavelengths of ~100 km. This suggests that, at 20-km horizontal resolution, the UWNMS is probably representing them reasonably well, but further resolution-dependent study is required to assess their fidelity.

In attempting to explain the orientation of the gravity wave phase axes, the V-shaped divergence patterns in the cross-jet section (Fig. 5d) may favor elongated gravity wave phase axes in that direction. It is also observed that the phase lines are perpendicular to the narrow arc of inertial instability in the middle and upper troposphere. A third contributing factor may be that selective wave transmissivity can yield a preferred propagation direction antiparallel to the prevailing wind, with phase axes perpendicular to the jet (Dunkerton and Butchart 1984). Eddy winds associated with gravity waves on the order of 10 m s^{-1} are sufficient to modulate the jet isosurface so as to cause this rib-like structure, which connects and modulates the two jets simultaneously. The visual impression is a stitching together or suturing of the two jets. This suggests that gravity waves excited by convection and inertial instability may influence the coevolution of proximal subpolar and subtropical jets.

Figure 8 shows a view from the east of the ascending negative PV streamers merging with downward-extending ''stalactites'' of high–wind speed air. This highlights the intimate connection between inertial instability and gravity wave generation in this simulation. Note the poleward and downward expansion of the jet isosurface from Fig. 8a through Fig. 8c as the region of inertially unstable air and high angular momentum surges poleward. Since the jet core exits the eastern model boundary, one may view snapshots of dollops of air with negative PV as they fly poleward into the subpolar jet, as the region of high wind speed bulges poleward and downward (cf. supplemental movie 3). A

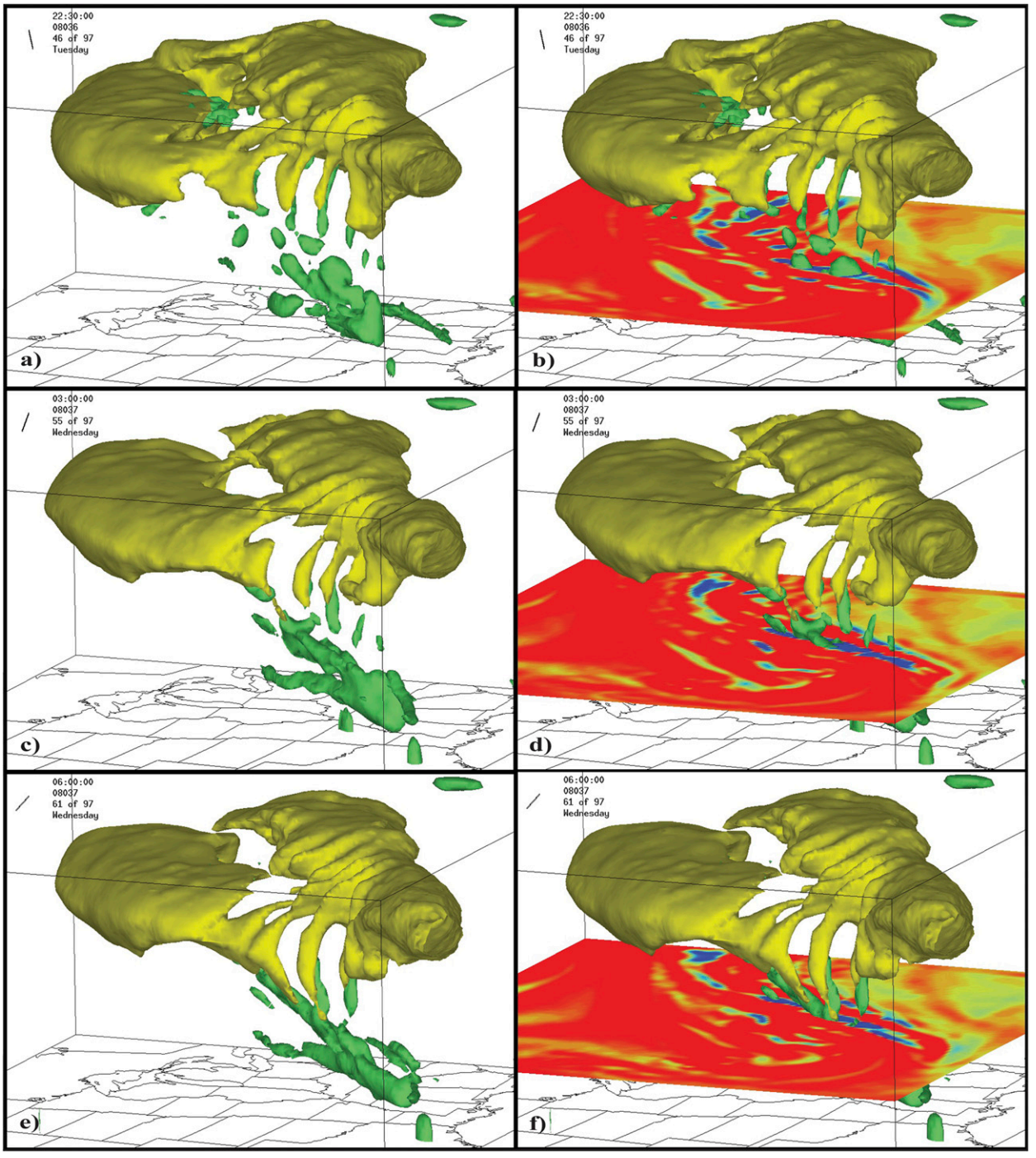

FIG. 7. View from the southwest of the influence of convection, inertial instability, and gravity waves on the subtropical and subpolar jets (55-m s^{-1} speed isosurfaces in yellow) in the UWNMS at (a),(b) 2230 UTC 5 ; (c),(d) 0300 UTC 6; and (e),(f) 0600 UTC 6 Feb 2008. The −1 PVU isosurfaces are shown in light green in each panel. (right) Absolute vorticity (10^{-5} s^{-1}) is included at 5 km (blue < 0; yellow 0–1; red > 1).

notable aspect of supplemental movies 2 and 3 is the appearance of a suturing of the two jets. To the extent that gravity waves break and mix, this may represent a mechanism of interaction between jets generated by convection and inertial instability.

5. Case study 2 (22 April 2005)

a. Synoptic overview

The spring storm of 22 April 2005, which caused significant precipitation across the Ohio valley also

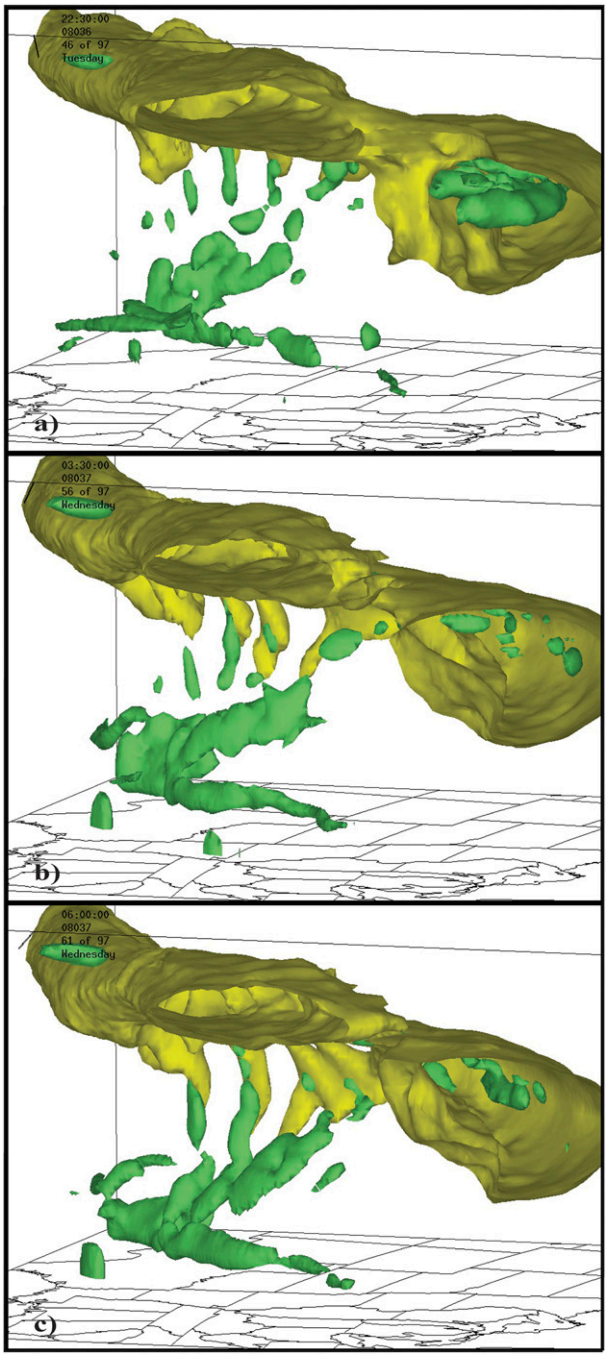

FIG. 8. As in Figs. 7a,c,e, but viewed from the east of inertially unstable air linked to gravity wave motions and poleward surges of the subpolar jet.

occurred between the subpolar and subtropical jets, ahead of an equatorward-extending stratospheric PV streamer (Figs. 9 and 10). Even though wind speeds were weaker than in Case 1, EPV still reached values of less than −2 PVU near 13 km. At 1200 UTC 22 April, a moderate low pressure system was found over the Ohio valley, advancing toward the northeast (Fig. 9a). Banded precipitation consistently formed and dissipated on the northwest side of the low pressure center, lingering into the late evening hours of 22 April 2005 (Fig. 9b). A subtropical westerly jet near 150 hPa (Fig. 9d) is seen extending from Southern California over Texas and toward the Gulf of Mexico, with a patch of inertial instability over Louisiana (negative PV in the 250–200-hPa layer in Fig. 9c). The subtropical westerly jet can also be seen at 300 hPa in Fig. 9f. Branches of the subpolar jet near 300 hPa can be seen extending from Manitoba southward toward Missouri and from southern Wisconsin arcing toward Nova Scotia (Fig. 9f). A meridionally oriented patch of negative EPV is seen over Indiana (Figs. 9e) on the anticyclonic-shear side of the subpolar jet just to the west of the surface low (Figs. 9f). Note also the negative EPV region equatorward of the subtropical westerly jet along the border with Mexico (Figs. 9e,f).

The region of inertial instability in the UTLS to the west of the surface low coincides with the westward extension of the precipitation maximum in Fig. 9b, consistent with previous findings that inertial instability can enhance rainfall in midlatitude cyclones. The existence of inertially unstable regions equatorward of westerly jets appears to occur frequently, with convection between two jets particularly conducive for inertial instability-driven poleward acceleration.

b. UWNMS simulation of Case 2 with GEOS ozone

The evolution of EPV (Figs. 10a,c,e) and GEOS ozone mixing ratio (Figs. 10b,d,f right) is shown, together with streamfunction in a meridional section extending from Georgia to southern Ontario, during 1200–2230 UTC 22 April 2005. EPV isosurfaces of −2 PVU are shown in green. High values of PV and ozone are indicated in red. Note the detailed agreement between the patterns of PV and ozone throughout the UTLS. The mesoscale structures of poleward deformation and stratospheric intrusion are created by the model physics in the UWNMS from coarser (2.5° resolution) initial fields. As with Case 1, the meridional streamfunction depicts a deep layer of poleward-moving air in the UTLS, which emanates from the convectively and inertially unstable updraft.

As the poleward surge in the large vault-like structure of negative PV progresses toward the Great Lakes in the UTLS, at lower levels a wedge of air descends and moves equatorward (sequence in Fig. 10). It underlies a thin layer of air with high PV, which extends downward and equatorward from the tropopause over Northern Michigan into the troposphere over Missouri. This differential advection can lead to the signature of a stratospheric intrusion.

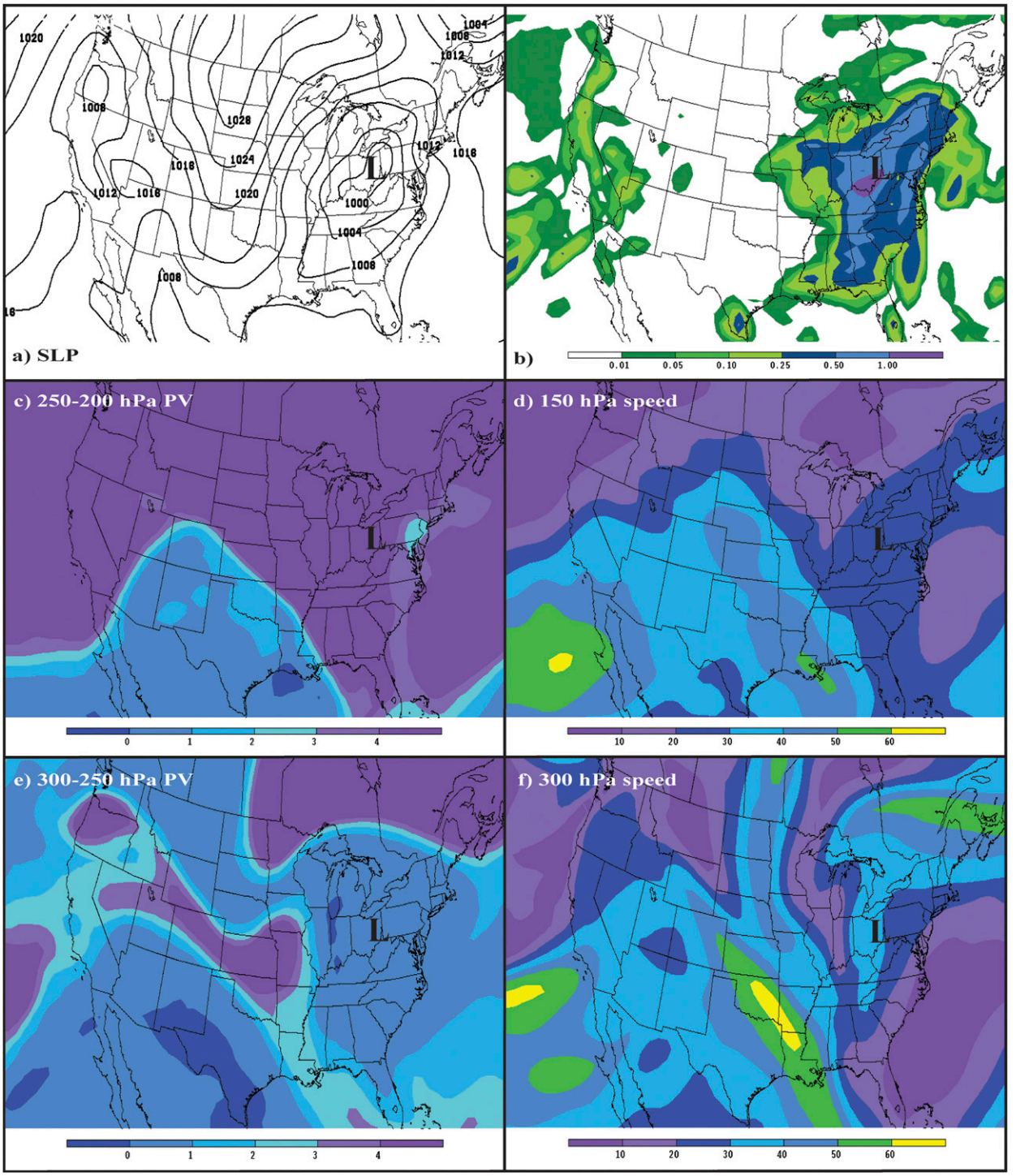

FIG. 9. Synoptic setting for Case 2, as shown in NCEP NAM model analyses at 1200 UTC 22 Apr 2005: (a) sea level pressure (gray contours; interval: 4 hPa), (b) 24-h accumulated precipitation during 0000 UTC 22–0000 UTC 23 Apr 2005 (color bar; inches), (c) 250–200-hPa PV (color bar; interval: 1 PVU), (d) 150-hPa speed (color bar; interval: 10 m s^{-1}. (e) 300–250-hPa PV, and (f) 300-hPa speed. The location of the surface low pressure center is indicated with an "L.".

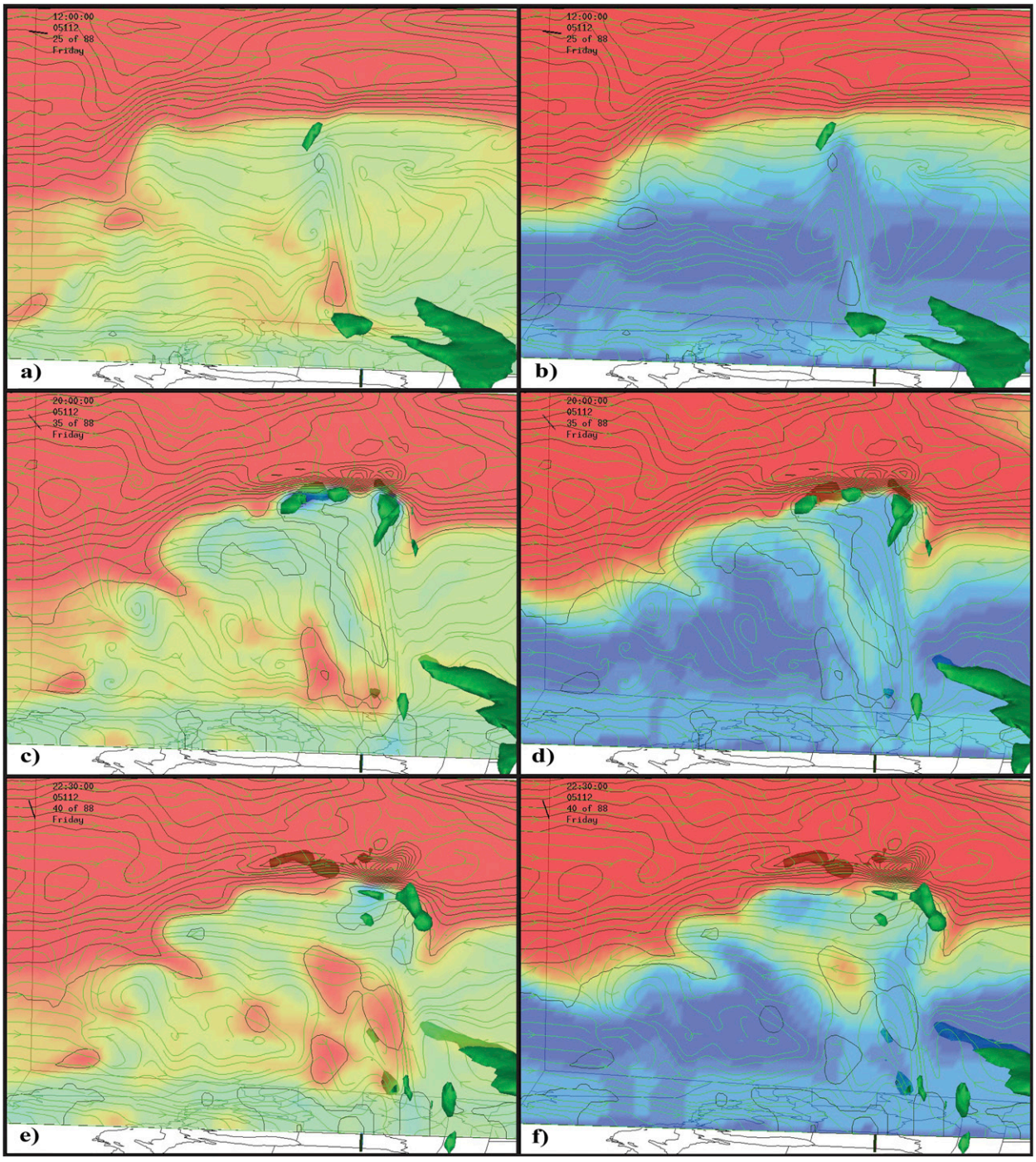

FIG. 10. Meridional sections in the UWNMS for Case 2 of (left) EPV (color) and (right) ozone mixing ratio (color) as the storm evolved from (a),(b) 1200 to (c),(d) 2000 UTC and (e)–(f) 2230 UTC 22 Apr 2005. Each panel includes contours of PV (gray; interval: 1 PVU), meridional streamfunction (green), and −2 PVU isosurfaces (light green). For EPV, blue < −1 PVU, yellow 1–2 PVU, and red > 2 PVU. For ozone, dark blue < 50 ppbv, light blue 50–100 ppbv, yellow 100–200 ppbv, and red > 200 ppbv.

This relationship between inertially unstable regions and stratospheric intrusions may also be seen acting at the mesoscale in association with the particular convective event over southern Indiana. Upon the convective injection of air with negative PV, indicated by the green isosurfaces near the tropopause in Figs. 10c–f, a mesoscale vault of tropospheric air is created, surrounded by a descending

sheet of stratospheric air, similar to the results of Hitchman et al. (2004).

The convective updraft over Indiana, as seen in the streamfunction, exhibits positive EPV production in the lower troposphere and negative EPV production in the upper troposphere, as a result of the latent heating maximum and associated vortex stretching in the lower troposphere and vortex compression in the upper troposphere (Figs. 10a,c,e). In contrast, the ozone field shows the simple pattern of low ozone values convected to the tropopause (cf. upward extension of light blue in Figs. 10b,d,f).

The development of sharp ozone structures in the UWNMS associated with negative PV regions lends further support to the idea that inertial instability can facilitate stratospheric intrusions. The structure in ozone and PV is consistent with upper-tropospheric air surging poleward over stratospheric air, yielding a trailing pattern of stratospheric intrusion underneath.

6. Summary of proposed mechanism

Two case studies have been presented that provide evidence for a causal relationship between inertial instability in the UTLS and locally enhanced STE near midlatitude westerly jets. This phenomenon occurs when a surface low pressure system, with associated convection along a cold frontal boundary, exists between a subtropical and subpolar jet, with WCB updrafts that lift the air to the base of the stratosphere, resulting in areas of enhanced inertial instability near the subpolar jet. It was shown that patterns of EPV, PV, and absolute vorticity coincide very closely in the UTLS, with negative values for each serving equally well as an indicator of inertial instability. The inertial instability facilitates poleward surges of air in the UTLS, which overrides stratospheric air. The vault of negative EPV and low Ri between the two jets is bordered by a locus of enhanced divergence/convergence with implied enhanced mixing and STE.

It is suggested that a stratospheric intrusion can be created simply by a vertically limited poleward surge in the UTLS, as shown schematically in Fig. 11. The poleward expansion of air in the uppermost troposphere over the underlying stratospheric air creates a stratospheric intrusion by simple kinematic folding through differential advection in the vertical. The boundaries of this poleward surge exhibit evidence of enhanced mixing (Fig. 5d) and, as with upright convection, a possible peripheral recirculation around the top and bottom of the poleward surge (Figs. 10c–f), as indicated by the small arrows in Fig. 11. Cases 1 and 2 show that this process can occur on a range of scales. In these cases, the poleward motion of rising light air advects the subtropical westerly jet northeastward over the equatorward-sinking cold air, as expected from sloping convection and baroclinic energy conversion in the RWB process.

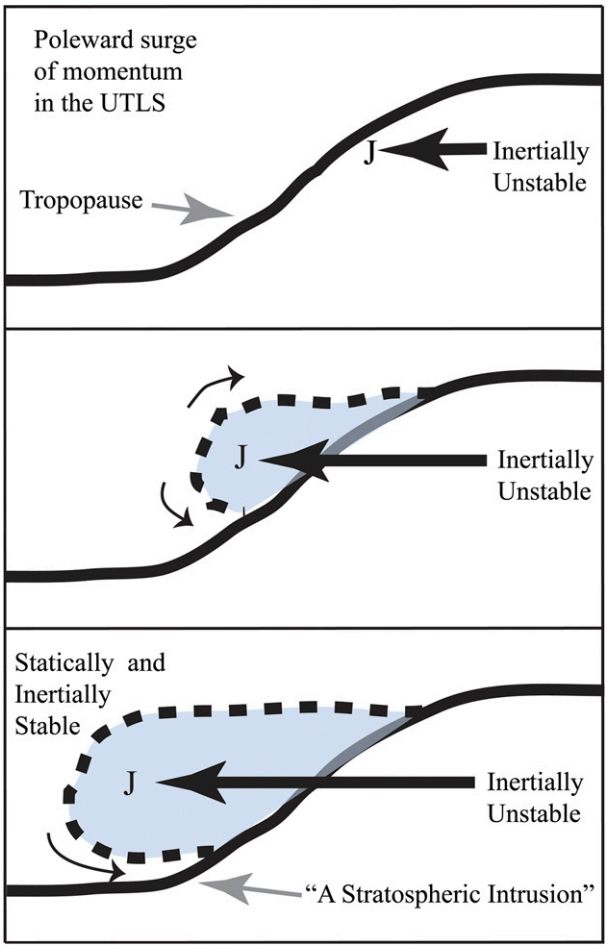

FIG. 11. Schematic diagram of a stratospheric intrusion formed by relative motion, in this case a poleward surge of air in the UTLS (time increases downward). Inertial instability aids the poleward intrusion of air, as the jet strengthens and moves poleward, overriding a thin layer of stratospheric air. The heavy dashed line indicates the displaced tropopause and is a locus of enhanced divergence–convergence and mixing of air. Recirculation around the nose of the poleward surge may aid filamentation of the intrusion, as suggested by the small arrows. Eventually, the lightness and inertial stability of the extratropical lower stratosphere limits further poleward motion.

It is found that inertial instability can act to accentuate poleward displacement in the WCB, promoting the large-scale baroclinic energy conversion by gravitational adjustment of air with differing density, constrained by the ridigity of planetary rotation. The poleward extension of the subtropical westerly jet is resisted by the enhanced meridional gradient of angular momentum (positive PV) of the extratropical lower stratosphere.

The gravity wave field excited by convective/inertial instability between the two jets modulates the two jets simultaneously, forming a rib-like connection between the two. Further work is required to diagnose the implications of this jet suture signature associated with the emanation of gravity waves from a narrow arc of inertial instability. We are currently exploring the seasonality and distribution of inertial instability influences on STE. A companion paper (S. M. Rowe and M. H. Hitchman 2015, unpublished manuscript) focuses on the relationship between inertial instability, divergence, poleward surges, and mesoscale jet flare ups.

Acknowledgments. We are grateful to the University of Wisconsin Alumni Research Foundation for providing the initial grant for pursuing this idea and for support from NASA Grant NNX10AG57G and NSF Grant AGS-1256215, which have allowed us to bring these ideas to fruition. We thank Ivanka Stajner for providing the GEOS ozone data for Case 2, Greg Tripoli and Zhengyu Liu for helpful conversations, and Pete Pokrandt and Marek Rogal for their technical expertise.

REFERENCES

Andrews, D. G., J. R. Holton, and C. B. Leovy, 1987: *Middle Atmosphere Dynamics*. Academic Press, 489 pp.

Bennetts, D. A., and B. J. Hoskins, 1979: Conditional symmetric instability—A possible explanation for frontal rainbands. *Quart. J. Roy. Meteor. Soc.,* **105,** 945–962, doi:10.1002/qj.49710544615.

Bowman, K. P., L. L. Pan, T. Campos, and R. Gao, 2007: Observations of fine-scale transport structure in the upper troposphere from the High-performance Instrumented Airborne Platform for Environmental Research. *J. Geophys. Res.,* **112,** D18111, doi:10.1029/2007JD008685.

Brennan, M. J., G. M. Lackmann, and K. M. Mahoney, 2008: Potential vorticity (PV) thinking in operations: The utility of nonconservation. *Wea. Forecasting,* **23,** 168–182, doi:10.1175/2007WAF2006044.1.

Browell, E. V., E. F. Danielsen, S. Ismail, G. L. Gregory, and S. M. Beck, 1987: Tropopause fold structure determined from airborne lidar in situ measurements. *J. Geophys. Res.,* **92,** 2112–2120, doi:10.1029/JD092iD02p02112.

Browning, K. A., and R. Reynolds, 1994: Diagnostic study of a narrow cold-frontal rainband and severe winds associated with a stratospheric intrusion. *Quart. J. Roy. Meteor. Soc.,* **120,** 235–257, doi:10.1002/qj.49712051602.

Büker, M. L., M. H. Hitchman, G. J. Tripoli, R. B. Pierce, E. V. Browell, and M. A. Avery, 2005: Resolution dependence of cross-tropopause ozone transport over East Asia. *J. Geophys. Res.,* **110,** D03107, doi:10.1029/2004JD004739.

——, ——, ——, ——, ——, and J. A. Al-Saadi, 2008: Long-range convective ozone transport during INTEX. *J. Geophys. Res.,* **113,** D14S90, doi:10.1029/2007JD009345.

Cao, Z., and H.-R. Cho, 1995: Generation of moist potential vorticity in extratropical cyclones. *J. Atmos. Sci.,* **52,** 3263–3281, doi:10.1175/1520-0469(1995)052<3263:GOMPVI>2.0.CO;2.

——, and D.-L. Zhang, 2004: Tracking surface cyclones with moist potential vorticity. *Adv. Atmos. Sci.,* **21,** 830–835, doi:10.1007/BF02916379.

Clayson, C. A., and L. Kantha, 2008: On turbulence and mixing in the free atmosphere inferred from high-resolution soundings. *J. Atmos. Oceanic Technol.,* **25,** 833–852, doi:10.1175/2007JTECHA992.1.

Cooper, O., and Coauthors, 2004: On the life cycle of a stratospheric intrusion and its dispersion into polluted warm conveyor belts. *J. Geophys. Res.,* **109,** D23S09, doi:10.1029/2003JD004006.

Danielsen, E. F., 1968: Stratospheric–tropospheric exchange based on radioactivity, ozone and potential vorticity. *J. Atmos. Sci.,* **25,** 502–518, doi:10.1175/1520-0469(1968)025<0502:STEBOR>2.0.CO;2.

Duck, T. J., and J. A. Whiteway, 2005: The spectrum of waves and turbulence at the tropopause. *Geophys. Res. Lett.,* **32,** L07801, doi:10.1029/2004GL021189.

Dunkerton, T. J., 1981: On the inertial stability of the equatorial middle atmosphere. *J. Atmos. Sci.,* **38,** 2354–2364, doi:10.1175/1520-0469(1981)038<2354:OTISFT>2.0.CO;2.

——, 1983: A nonsymmetric equatorial inertial instability. *J. Atmos. Sci.,* **40,** 807–813, doi:10.1175/1520-0469(1983)040<0807:ANEII>2.0.CO;2.

——, and N. Butchart, 1984: Propagation and selective transmission of internal gravity waves in a sudden warming. *J. Atmos. Sci.,* **41,** 1443–1460, doi:10.1175/1520-0469(1984)041<1443:PASTOI>2.0.CO;2.

Eliassen, A., and E. Kleinschmidt, 1957: Dynamic meteorology. *Geophysics II,* J. Bartels, Ed., Encyclopedia of Physics, 48, Springer-Verlag, 1–154.

Emanuel, K. A., 1979: Inertial instability and mesoscale convective systems. Part I: Linear theory of inertial instability in rotating, viscous fluids. *J. Atmos. Sci.,* **36,** 2425–2449, doi:10.1175/1520-0469(1979)036<2425:IIAMCS>2.0.CO;2.

Griffiths, M., A. J. Thorpe, and K. A. Browning, 2000: Convective destabilization by a tropopause fold diagnosed using potential-vorticity inversion. *Quart. J. Roy. Meteor. Soc.,* **126,** 125–144, doi:10.1002/qj.49712656207.

Halcomb, C. E., and P. S. Market, 2003: Forcing, instability and equivalent potential vorticity in a Midwest USA convective snowstorm. *Meteor. Appl.,* **10,** 273–280, doi:10.1017/S1350482703003074.

Hayashi, H., M. Shiotani, and J. Gille, 2002: Horizontal wind disturbances induced by inertial instability in the equatorial middle atmosphere as seen in rocketsonde observations. *J. Geophys. Res.,* **107,** 4228, doi:10.1029/2001JD000922.

Haynes, P. H., C. J. Marks, M. E. McIntyre, T. G. Shepherd, and K. P. Shine, 1991: On the ''downward control'' of extratropical diabatic circulations by eddy-induced mean zonal forces. *J. Atmos. Sci.,* **48,** 651–678, doi:10.1175/1520-0469(1991)048<0651:OTCOED>2.0.CO;2.

Hegglin, M. I., and Coauthors, 2008: Validation of ACE-FTS satellite data in the upper troposphere/lower stratosphere (UTLS) using non-coincident measurements. *Atmos. Chem. Phys.,* **8,** 1483–1499, doi:10.5194/acp-8-1483-2008.

Hitchman, M. H., and C. B. Leovy, 1986: Evolution of the zonal mean state in the equatorial middle atmosphere during October 1978–May 1979. *J. Atmos. Sci.,* **43,** 3159–3176, doi:10.1175/1520-0469(1986)043<3159:EOTZMS>2.0.CO;2.

——, ——, J. C. Gille, and P. L. Bailey, 1987: Quasi-stationary zonally asymmetric circulations in the equatorial lower mesosphere. *J. Atmos. Sci.,* **44,** 2219–2236, doi:10.1175/1520-0469(1987)044<2219:QSZACI>2.0.CO;2.

——, M. L. Büker, and G. J. Tripoli, 1999: Influence of synoptic waves on column ozone during Arctic summer 1997. *J. Geophys. Res.,* **104,** 26 547–26 563, doi:10.1029/1999JD900471.

——, ——, ——, E. V. Browell, W. B. Grant, C. Hostetler, T. J. McGee, and J. F. Burris, 2003: Nonorographic generation of Arctic polar stratospheric clouds during December 1999. *J. Geophys. Res.,* **108,** 8325, doi:10.1029/2001JD001034.

——, ——, ——, R. B. Pierce, J. A. Al-Saadi, E. V. Browell, and M. A. Avery, 2004: A modeling study of an East Asian convective complex during March 2001. *J. Geophys. Res.,* **109,** D15S14, doi:10.1029/2003JD004312.

Hoggatt, B. D., and J. A. Knox, 1998: Non-hydrostatic simulation of unforecast convection in an intense mid-latitude anticyclone. Preprints, *12th Conf. on Numerical Weather Prediction,* Phoenix, AZ, Amer. Meteor. Soc., 59–62.

Holton, J. R., 2006: *An Introduction to Dynamic Meteorology.* Academic Press, 535 pp.

——, P. H. Haynes, M. E. McIntyre, A. R. Douglass, R. B. Rood, and L. Pfister, 1995: Stratosphere–troposphere exchange. *Rev. Geophys.,* **33,** 403–439, doi:10.1029/95RG02097.

Homeyer, C. R., K. P. Bowman, L. L. Pan, M. A. Zondlo, and J. F. Bresch, 2011: Convective injection into stratospheric intrusions. *J. Geophys. Res.,* **116,** D23304, doi:10.1029/2011JD016724.

Hoor, P., H. Fischer, L. Lange, J. Lelieveld, and D. Brunner, 2002: Seasonal variations of a mixing layer in the lowermost stratosphere as identified by the CO–O_3 correlation from in situ measurements. *J. Geophys. Res.,* **107,** 4044, doi:10.1029/2000JD000289.

Hoskins, B. J., M. E. McIntyre, and A. W. Robertson, 1985: On the use and significance of isentropic potential vorticity maps. *Quart. J. Roy. Meteor. Soc.,* **111,** 877–946, doi:10.1002/qj.49711147002.

Jones, S. C., and A. J. Thorpe, 1992: The three-dimensional nature of 'symmetric' instability. *Quart. J. Roy. Meteor. Soc.,* **118,** 227–258, doi:10.1002/qj.49711850404.

Joos, H., and H. Wernli, 2012: Influence of microphysical processes on the potential vorticity development in a warm conveyor belt: A case-study with the limited-area model COSMO. *Quart. J. Roy. Meteor. Soc.,* **138,** 407–418, doi:10.1002/qj.934.

Kittaka, C., and Coauthors, 2004: A three-dimensional regional modeling study of the impact of clouds on sulfate distributions during TRACE-P. *J. Geophys. Res.,* **109,** D15S11, doi:10.1029/2003JD004353.

Knippertz, P., and H. Wernli, 2010: A Lagrangian climatology of tropical moisture exports to the Northern Hemispheric extratropics. *J. Climate,* **23,** 987–1003, doi:10.1175/2009JCLI3333.1.

Knox, J. A., 1997: Possible mechanisms of clear-air turbulence in strongly anticyclonic flows. *Mon. Wea. Rev.,* **125,** 1251–1259, doi:10.1175/1520-0493(1997)125<1251:PMOCAT>2.0.CO;2.

——, 2003: Inertial instability. *Encyclopedia of the Atmospheric Sciences,* 1st ed. J. Holton, J. Pyle, and J. Curry, Eds., Academic Press, 1004–1013.

——, and V. L. Harvey, 2005: Global climatology of inertial instability and Rossby wave breaking in the stratosphere. *J. Geophys. Res.,* **110,** D06108, doi:10.1029/2004JD005068.

Koch, S. E., and Coauthors, 2005: Turbulence and gravity waves within an upper-level front. *J. Atmos. Sci.,* **62,** 3885–3908, doi:10.1175/JAS3574.1.

Lang, A. A., 2011: The structure and evolution of lower stratospheric frontal zones. Ph. D. dissertation, University of Wisconsin–Madison, 106 pp. [Available from Department of Atmospheric and Oceanic Sciences, University of Wisconsin–Madison, 1225 W. Dayton Street, Madison, WI 53706.]

——, and J. E. Martin, 2010: The influence of rotational frontogenesis and its associated shearwise vertical motions on the development of an upper-level front. *Quart. J. Roy. Meteor. Soc.,* **136,** 239–252, doi:10.1002/qj.551.

Lindzen, R. S., and K.-K. Tung, 1976: Banded convective activity and ducted gravity waves. *Mon. Wea. Rev.,* **104,** 1602–1617, doi:10.1175/1520-0493(1976)104<1602:BCAADG>2.0.CO;2.

Madonna, E., H. Wernli, H. Joos, and O. Martius, 2014: Warm conveyor belts in the ERA-Interim dataset (1979–2010). Part I: Climatology and potential vorticity evolution. *J. Climate,* **27,** 3–26, doi:10.1175/JCLI-D-12-00720.1.

Manabe, S., and R. T. Wetherald, 1967: Thermal equilibrium of the atmosphere with a given distribution of relative humidity. *J. Atmos. Sci.,* **24,** 241–259, doi:10.1175/1520-0469(1967)024<0241:TEOTAW>2.0.CO;2.

Markowski, P., and Y. Richardson, 2010: *Mesoscale Meteorology in Midlatitudes.* John Wiley and Sons, 407 pp.

Martin, J. E., 2006: The role of shearwise and transverse quasigeostrophic vertical motions in the midlatitude cyclone life cycle. *Mon. Wea. Rev.,* **134,** 1174–1193, doi:10.1175/MWR3114.1.

McIntyre, M. E., and T. N. Palmer, 1983: Breaking planetary waves in the stratosphere. *Nature,* **305,** 593–600, doi:10.1038/305593a0.

Montgomery, M. T., and B. F. Farrell, 1991: Moist surface frontogenesis associated with interior potential vorticity anomalies in a semigeostrophic model. *J. Atmos. Sci.,* **48,** 343–368, doi:10.1175/1520-0469(1991)048<0343:MSFAWI>2.0.CO;2.

Morgan, M. C., 1999: Using piecewise potential vorticity inversion to diagnose frontogenesis. Part I: A partitioning of the Q vector applied to diagnosing surface frontogenesis and vertical motion. *Mon. Wea. Rev.,* **127,** 2796–2821, doi:10.1175/1520-0493(1999)127<2796:UPPVIT>2.0.CO;2.

O'Sullivan, D. J., 1993: Inertial instability and inertia–gravity wave generation in the midlatitude winter stratosphere. Preprints, *Ninth Conf. on Atmospheric and Oceanic Waves and Stability,* San Antonio, TX, Amer. Meteor. Soc., 96–97.

——, and M. H. Hitchman, 1992: Inertial instability and Rossby wave breaking in a numerical model. *J. Atmos. Sci.,* **49,** 991–1002, doi:10.1175/1520-0469(1992)049<0991:IIARWB>2.0.CO;2.

——, and T. J. Dunkerton, 1995: Generation of inertia–gravity waves in a simulated life cycle of baroclinic instability. *J. Atmos. Sci.,* **52,** 3695–3716, doi:10.1175/1520-0469(1995)052<3695:GOIWIA>2.0.CO;2.

Pan, L. L., and Coauthors, 2007: Chemical behavior of the tropopause observed during the stratosphere–troposphere analyses of regional transport experiment. *J. Geophys. Res.,* **112,** D18110, doi:10.1029/2007JD008645.

Pavelin, E., J. Whiteway, R. Busen, and J. Hacker, 2002: Airbourne observations of turbulence, mixing, and gravity waves in the tropopause region. *J. Geophys. Res.,* **107,** doi:10.1029/2001JD000775.

Pokrandt, P. J., G. J. Tripoli, and D. D. Houghton, 1996: Processes leading to the formation of mesoscale waves in the Midwest cyclone of 15 December 1987. *Mon. Wea. Rev.,* **124,** 2726–2752, doi:10.1175/1520-0493(1996)124<2726:PLTTFO>2.0.CO;2.

Pomroy, H. R., and A. J. Thorpe, 2000: The evolution and dynamical role of reduced upper-tropospheric potential vorticity in Intensive Observing Period One of FASTEX. *Mon. Wea. Rev.,* **128,** 1817–1834, doi:10.1175/1520-0493(2000)128<1817:TEADRO>2.0.CO;2.

Randel, W. J., D. J. Seidel, and L. L. Pan, 2007: Observational characteristics of double tropopauses. *J. Geophys. Res.,* **112,** D07309, doi:10.1029/2006JD007904.

Rayleigh, L., 1917: On the dynamics of revolving fluids. *Proc. Roy. Soc. London,* **93A,** 148–154.

Sato, K., and T. J. Dunkerton, 2002: Layered structure associated with low potential vorticity near the tropopause seen in high-resolution radiosondes over Japan. *J. Atmos. Sci.,* **59,** 2782–2800, doi:10.1175/1520-0469(2002)059<2782:LSAWLP>2.0.CO;2.

Sawyer, J. S., 1949: The significance of dynamic instability in atmospheric motions. *Quart. J. Roy. Meteor. Soc.,* **75,** 364–374, doi:10.1002/qj.49707532604.

Schemm, S., H. Wernli, and L. Papritz, 2013: Warm conveyor belts in idealized moist baroclinic wave simulations. *J. Atmos. Sci.,* **70,** 627–652, doi:10.1175/JAS-D-12-0147.1.

Schoeffler, F. S., 2013: Large wildfire growth influenced by tropospheric and stratospheric dry slots in the United States. *17th Conf. on the Middle Atmosphere,* Newport, RI, 5.1. [Available online at https://ams.confex.com/ams/19Fluid17Middle/webprogram/Paper225271.html.]

Schultz, D. M., and J. A. Knox, 2007: Banded convection caused by frontogenesis in a conditionally, symmetrically, and inertially unstable environment. *Mon. Wea. Rev.,* **135,** 2095–2110, doi:10.1175/MWR3400.1.

Schumacher, R. S., and D. M. Schultz, 2000: Inertial instability: Climatologies and possible relationship to severe weather predictability. Preprints, *Ninth Conf. on Mesoscale Processes,* Fort Lauderdale, FL, Amer. Meteor. Soc., P4.17. [Available online at https://ams.confex.com/ams/WAF-NWP-MESO/techprogram/paper_22733.htm.]

——, ——, and J. A. Knox, 2010: Convective snowbands downstream of the Rocky Mountains in an environment with conditional, dry symmetric, and inertial instabilities. *Mon. Wea. Rev.,* **138,** 4416–4438, doi:10.1175/2010MWR3334.1.

——, ——, and ——, 2015: Influence of terrain resolution on banded convection in the lee of the Rocky Mountains. *Mon. Wea. Rev.,* **143,** 1397–1414, doi:10.1175/MWR-D-14-00255.1.

Shapiro, M. A., 1974: A multiple structured frontal zone-jet stream system as revealed by meteorologically instrumented aircraft. *Mon. Wea. Rev.,* **102,** 244–253, doi:10.1175/1520-0493(1974)102<0244:AMSFZJ>2.0.CO;2.

——, 1978: Further evidence of the mesoscale and turbulent structure of upper level jet stream–frontal zone systems. *Mon. Wea. Rev.,* **106,** 1100–1111, doi:10.1175/1520-0493(1978)106<1100:FEOTMA>2.0.CO;2.

——, 1980: Turbulent mixing within tropopause folds as a mechanism for the exchange of chemical constituents between the stratosphere and troposphere. *J. Atmos. Sci.,* **37,** 994–1004, doi:10.1175/1520-0469(1980)037<0994:TMWTFA>2.0.CO;2.

——, 1981: Frontogenesis and geostrophically forced secondary circulations in the vicinity of jet stream–frontal zone systems. *J. Atmos. Sci.,* **38,** 954–972, doi:10.1175/1520-0469(1981)038<0954:FAGFSC>2.0.CO;2.

——, 1985: Dropwindsonde observations of an Icelandic low and a Greenland mountain-lee wave. *Mon. Wea. Rev.,* **113,** 680–683, doi:10.1175/1520-0493(1985)113<0680:DOOAIL>2.0.CO;2.

——, T. Hampel, and A. J. Krueger, 1987: The Arctic tropopause fold. *Mon. Wea. Rev.,* **115,** 444–454, doi:10.1175/1520-0493(1987)115<0444:TATF>2.0.CO;2.

Smith, K. S., and E. Bernard, 2013: Geostrophic turbulence near rapid changes in stratification. *Phys. Fluids,* **25,** 046601, doi:10.1063/1.4799470.

Stajner, I., and Coauthors, 2008: Assimilated ozone from EOS-Aura: Evaluation of the tropopause region and tropospheric columns. *J. Geophys. Res.,* **113,** D16S32, doi:10.1029/2007JD008863.

Stevens, D. E., and P. E. Ciesielski, 1986: Inertial instability of horizontally sheared flow away from the equator. *J. Atmos. Sci.,* **43,** 2845–2856, doi:10.1175/1520-0469(1986)043<2845:IIOHSF>2.0.CO;2.

Stohl, A., and Coauthors, 2003: Stratosphere–troposphere exchange: A review, and what we have learned from STACCATO. *J. Geophys. Res.,* **108,** 8516, doi:10.1029/2002JD002490.

Stull, R. B., 1988: *An Introduction to Boundary Layer Meteorology.* Springer, 666 pp.

Taylor, G. I., 1923: Stability of a viscous liquid contained between two rotating cylinders. *Philos. Trans. Roy. Soc. London,* **223A,** 289–343, doi:10.1098/rsta.1923.0008.

Thorncroft, C. D., B. J. Hoskins, and M. E. McIntyre, 1993: Two paradigms of baroclinic-wave life-cycle behavior. *Quart. J. Roy. Meteor. Soc.,* **119,** 17–55, doi:10.1002/qj.49711950903.

Tripoli, G. J., 1992a: An explicit three-dimensional nonhydrostatic numerical simulation of a tropical cyclone. *Meteor. Atmos. Phys.,* **49,** 229–254, doi:10.1007/BF01025409.

——, 1992b: A nonhydrostatic numerical model designed to simulate scale interaction. *Mon. Wea. Rev.,* **120,** 1342–1359, doi:10.1175/1520-0493(1992)120<1342:ANMMDT>2.0.CO;2.

Uccellini, L. W., and S. E. Koch, 1987: The synoptic and possible energy sources for mesoscale wave disturbances. *Mon. Wea. Rev.,* **115,** 721–729, doi:10.1175/1520-0493(1987)115<0721:TSSAPE>2.0.CO;2.

Whiteway, J. A., E. G. Pavelin, R. Busen, J. Hacker, and S. Vosper, 2003: Airborne measurements of gravity wave breaking at the tropopause. *Geophys. Res. Lett.,* **30,** 2070, doi:10.1029/2003GL018207.

Wicker, L. J., and W. C. Skamarock, 1998: A time-splitting scheme for the elastic equations incorporating second-order Runge–Kutta time differencing. *Mon. Wea. Rev.,* **126,** 1992–1999, doi:10.1175/1520-0493(1998)126<1992:ATSSFT>2.0.CO;2.

Zahn, A., and Coauthors, 2000: Identification of extratropical two-way troposphere–stratosphere mixing based on CARIBIC measurements of O_3, CO, and ultrafine particles. *J. Geophys. Res.,* **105,** 1527–1535, doi:10.1029/1999JD900759.

Zhang, D.-L., and H.-R. Cho, 1992: The development of negative moist potential vorticity in the stratiform region of a simulated squall line. *Mon. Wea. Rev.,* **120,** 1322–1341, doi:10.1175/1520-0493(1992)120<1322:TDONMP>2.0.CO;2.

Zimet, T. K., J. E. Martin, and B. E. Potter, 2007: The influence of an upper-level frontal zone on the Mack Lake wildfire environment. *Meteor. Appl.,* **14,** 131–147, doi:10.1002/met.14.